IEEE Access
Multidisciplinary ⋮ Rapid Review ⋮ Open Access Journal

Received 4 March 2025, accepted 6 April 2025, date of publication 10 April 2025, date of current version 17 April 2025.

Digital Object Identifier 10.1109/ACCESS.2025.3559146

RESEARCH ARTICLE

Analytical Optimal Control of Delayed Worm Propagation Model in Heterogeneous IoT Systems

B. S. N. MURTHY[1], V. MADHUSUDANAN[2], M. N. SRINIVAS[3], L. GUERRINI[4], ANWAR ZEB[5], NHU-NGOC DAO[6], (Senior Member, IEEE), AND SUNGRAE CHO[7]

[1]Department of Mathematics, Aditya University, Surampalem, Andhra Pradesh 533437, India
[2]Department of Mathematics, S. A. Engineering College, Chennai, Tamil Nadu 600077, India
[3]Department of Mathematics, School of Advanced Sciences, Vellore Institute of Technology, Vellore, Tamil Nadu 632014, India
[4]Department of Management, Polytechnic University of Marche, 60121 Ancona, Italy
[5]Department of Mathematics, COMSATS University Islamabad, Abbottabad, Khyber Pakhtunkhwa 22060, Pakistan
[6]Department of Computer Science and Engineering, Sejong University, Seoul 05006, South Korea
[7]School of Computer Science and Engineering, Chung-Ang University, Seoul 06974, South Korea

Corresponding authors: Nhu-Ngoc Dao (nndao@sejong.ac.kr) and Sungrae Cho (srcho@cau.ac.kr)

This work was supported in part by the Institute of Information and Communications Technology Planning and Evaluation (IITP) through the Information Technology Research Center (ITRC), 50% grant funded by Korean Government of the Ministry of Science and ICT (MSIT) under Grant IITP-2025-RS-2022-00156353; and in part by the IITP under YKCS Open RAN Global Collaboration Research Center grant funded by Korean Government (MSIT) under Grant IITP-2025-RS-2024-00434743.

ABSTRACT This paper presents a mathematical model for worm propagation, where infectivity is influenced by latency within heterogeneous Internet of Things (IoT) systems. The model incorporates the heterogeneity of susceptible-exposed-infected-recovered (SEIR) compartments and considers the varying negative impacts of worms spread across these groups. Sufficient conditions for the persistence of worm propagation are derived using the optimistic equilibrium point. By selecting latency as a bifurcation parameter, the study reveals a specific latency value critical for maintaining worm propagation's stability in these systems. The normal form approach and central manifold theory are employed to analyze the direction and stability of Hopf bifurcation. Furthermore, this study addresses strategies for mitigating the spread of worms by employing best practices to minimize the number of devices exposed and infected across systems. We analyze the effects of control measures, such as vaccination and treatment, which should be applied promptly during a worm proliferation outbreak and gradually scaled down over time as the outbreak decreases. Numerical findings expose that latency significantly impacts system stability, however, optimally managing the latency below a deterministic threshold may maintain system stabilization.

INDEX TERMS Internet of Things, time delay, Hopf bifurcation, optimal control.

I. INTRODUCTION

A. MOTIVATIONS

The Heterogeneous Internet of Things (HIoT) is a network of physical equipment, vehicles, and electronic devices, including sensors, software, and connection. These objects can connect, collect, and share data without the need for human interaction. Human-to-human communication refers to the exchange of information between two or more individuals. In contrast, human-to-human interaction with the computer involves the interaction between a person and a computer system. Meanwhile, HIoT devices such as sensors, actuators, and smart appliances are vulnerable to malware infiltration due to their low cost and short time to market. Furthermore, most of HIoT devices are not regularly maintained and are left to run on customer property. However, most HIoT devices are set up and operated by users with little security experience. Customers may agree to install

The associate editor coordinating the review of this manuscript and approving it for publication was Ting Yang.

specific programs or processes on their devices in exchange for rewards, without being aware that doing so could lead to an attack. The subsequent points of view are used in academic research on malware spread, such as mathematical modeling and detection technology. The proliferation of the Internet of Things (IoT) has raised concerns about the increasing impact of malicious code due to its limitations in computing and communication capabilities [1], [2]. In particular, HIoT systems are susceptible to malicious code attacks due to their unique characteristics, such as limited bandwidth and inadequate protection. HIoTs typically consist of numerous heterogeneous nodes structured ad hoc to monitor their surroundings, often placing them at physical risk. Thus, a comprehensive examination of the propagation dynamics of malicious code is crucial to enhance the security of HIoTs. Because of infectious diseases and malware in heterogeneous IoT are so similar, epidemiology-built models explaining the spread of infectious diseases can be used to investigate the dynamics of malware propagation in heterogeneous IoT. These models help us predict how and to what extent malware will spread in the future across heterogeneous IoT. To help administrators create malware countermeasures, they also help us illustrate the effect elements determining whether the malware will spread or dissipate in heterogeneous IoT.

Malware can be launched by one IoT device and spread to another, and its hostile activities in the HIoT network naturally extend to physical threats. Due to a lack of technical implementation experience and vulnerabilities that arise in various technologies, such as IPv6 or the IoTs, malware can spread through propagation vectors such as services or functions. Consequently, it is challenging to identify and monitor the propagation process. Modeling techniques are used to forecast propagation dynamics and investigate influencing factors based on our knowledge of the technology and experience with previous attacks. A key concern is the development of accurate mathematical models to better understand the dynamics of malicious code propagation [3], [4], [5], [6], [7]. This is achieved by establishing compelling similarities between malicious codes and their natural counterparts.

B. LITERATURE REVIEW

In recent years, researchers have developed and examined various mathematical models to investigate the spread of malicious code in HIoTs. Various strategies have been proposed to extend the lifespan of HIoTs, focusing on reducing power usage [8], [9], [10], optimizing device placement [11], and managing the system topology [12]. Due to their limited resources, the HIoT nodes have vulnerable defenses and are susceptible to worm attacks.

Researchers have used epidemic models to analyze the behavior of malicious entities on the Internet, providing valuable information on the management of worm propagation within systems [13], [14], [15], [16], [17], [18]. For example, the authors in [15] presented a model for email viruses that considered user behavior and examined the spread patterns of email viruses in various system structures.

As harmful code propagates through a system, it incurs multiple types of delay, such as immunity delay, propagation delay, and virus cleanup delay. Keshri and Mishra [19] conducted a comprehensive analysis of a dynamic model that examined the transmission of harmful signals in a HIoT. Their model incorporated both transient and immunity delays, demonstrating that these delays could impact harmful attack management. Zizhen et al. [20] investigated Hopf bifurcation phenomena with time delay in a computer virus model, considering external computer influences and employing latency as a branching parameter. Zhao et al. [21] studied an SEIR computer virus model with delayed propagation and limited antivirus capabilities, evaluating how virus cleanup delays affect the model. Wang and Chai [22] explored the Hopf bifurcation in a delayed SEIRS model, analyzing the interplay of latency and transient immunity as branching parameters. Khan et al. [23] introduced a social networking addiction model incorporating saturation incidence and latency during transient immunity, further investigating Hopf stability and branching in this context.

C. PROBLEM STATEMENT

Different from the aforementioned works, this paper proposes a delayed HSEIR model for worm propagation in HIoT systems. The system consists of four compartments: susceptible (S), exposed (E), infected (I), and recovered (R), at time (t). We assume that the ratio of HIoT devices infected by nodes with limited spreading skills is σ and the ratio of HIoT devices infected by nodes with strong spreading capabilities is $1-\sigma$. The susceptible devices transition to the exposed state, with new exposures at time t are given by the expression $\sigma\beta SI + (1-\sigma)\lambda SI$, where β and λ are the transmission coefficients for devices with weak and strong spreading capabilities in the IoT system, respectively. Let δ denote the transition rate from exposed devices to infected devices when the worm becomes active in the IoT system. Let α, γ and θ represent the proportions of susceptible, exposed, and infectious devices that recover at time t, respectively. The worm-induced death rate for IoT devices is η, and the natural death rates for devices in the IoT system are μ_1, μ_2, μ_3 and μ_4.

Qing et al. [24] studied the stability of the system without considering the delay

$$\begin{aligned}
\dot{S} &= \Pi - \sigma\beta SI - (1-\sigma)\lambda SI - \alpha S - \mu_1 S,\\
\dot{E} &= \sigma\beta SI + (1-\sigma)\lambda SI - \delta E - \gamma E - \mu_2 E,\\
\dot{I} &= \delta E - \theta I - \eta I - \mu_3 I,\\
\dot{R} &= \alpha S + \gamma E + \theta I - \mu_4 R. \qquad (1)
\end{aligned}$$

As demonstrated in [23], worm transmission in IoT systems typically involve delay. Due to worms' internal latency, a delay often occurs between the infection of exposed devices and their capability to infect others. Lag differential equations exhibit more intricate dynamics than ordinary differential

equations. This lag can induce Hopf bifurcation phenomena, altering the behavior of the dynamical system and causing a shift from stable focus to cyclical boundaries [24], [25], [26], [27], [28], [29]. Therefore, this study investigates the complex dynamics of system (1) and emphasizes the critical role of time delays, particularly the Hopf branch, in controlling worm propagation in HIoT systems. The modified system with delay is as follows

$$\begin{aligned}
\dot{S} &= \Pi - \sigma\beta SI - (1-\sigma)\lambda SI - \alpha S - \mu_1 S,\\
\dot{E} &= \sigma\beta SI + (1-\sigma)\lambda SI - \delta E(t-\tau) - \gamma E - \mu_2 E,\\
\dot{I} &= \delta E(t-\tau) - \theta I - \eta I - \mu_3 I,\\
\dot{R} &= \alpha S + \gamma E + \theta I - \mu_4 R,
\end{aligned} \tag{2}$$

where τ is the worm incubation period in the IoT system. The removal of worms from infected IoT systems by antivirus software often requires significant time, necessitating consideration of latency caused by antivirus eradication processes. By focusing on the first three equations of (1), we obtain the simplified system

$$\begin{aligned}
\dot{S} &= \Pi - \sigma\beta SI - (1-\sigma)\lambda SI - \alpha S - \mu_1 S,\\
\dot{E} &= \sigma\beta SI + (1-\sigma)\lambda SI - \delta E(t-\tau) - \gamma E - \mu_2 E,\\
\dot{I} &= \delta E(t-\tau) - \theta I - \eta I - \mu_3 I.
\end{aligned} \tag{3}$$

D. OUR CONTRIBUTIONS

The primary objective of our study is to examine the impact of delay on system (3) and identify the optimal delay threshold, where the system can maintain stability under a worm propagation issue. The contributions in this paper are described as follows.

- Necessary conditions for local stability and the occurrence of a local Hopf bifurcation are analyzed, with the delay caused by the latent period of worm propagation from an exposed device to an infected one within an HIoT system used as the bifurcation parameter. The normal form technique and the center manifold theorem are used to determine the direction of the Hopf bifurcation and the stability of the bifurcating periodic solutions, see Sections II and III.
- Based on the above investigation, the optimal delay period required to maintain stability in system (3) is specified. In addition, we apply Pontryagin's maximum principle to characterize optimal control of worm propagation within the IoT system. The theoretical analysis is supported by numerical results obtained by an extensive simulation, see Sections IV–VI.

II. STABILITY AND HOPF BIFURCATION

This section mainly addresses the local stability of the positive equilibrium and the conditions for the presence of a local Hopf bifurcation. The communication radius can be determined by computing the matrices F and V, which are defined as follows

$$F = \begin{bmatrix} 0 & \dfrac{\Pi\left[\sigma\beta + (1-\sigma)\lambda\right]}{\alpha+\mu_1} \\ 0 & 0 \end{bmatrix},$$

$$V = \begin{bmatrix} \delta+\gamma+\mu_2 & 0 \\ -\delta & \theta+\mu_3 \end{bmatrix}.$$

The communication radius is defined as the dominant eigenvalue of FV^{-1}, leading to the expression

$$R_0 = \rho(FV^{-1}) = \frac{\Pi\delta\left(\sigma\beta + (1-\sigma)\lambda\right)}{(\alpha+\mu_1)(\delta+\gamma+\mu_2)(\theta+\mu_3+\xi)}.$$

This formulation provides a measure of how the information propagates within the system. Our system has a positive equilibrium P^* (S^*, E^*, I^*, R^*), where

$$S^* = \frac{\Pi}{(\sigma\beta+\lambda-\sigma\lambda)I^* + (\mu_1+\alpha)},$$

$$E^* = \frac{\mu_3+\theta+\eta}{\delta} I^*,$$

$$I^* = \frac{(R_0-1)(\mu_1+\alpha)}{\sigma\beta+\lambda-\sigma\lambda},$$

$$R^* = \frac{\gamma E^* + \theta I^* + \alpha S^*}{\mu_4}.$$

The linearization of (3) at P^* (S^*, E^*, I^*, R^*) is

$$\begin{aligned}
\dot{S}(t) &= a_1 S(t) + a_2 I(t),\\
\dot{E}(t) &= a_3 S(t) + a_4 E(t) + a_5 E(t) + b_1 E(t-\tau),\\
\dot{I}(t) &= b_2 E(t-\tau) + a_6 I(t),
\end{aligned} \tag{4}$$

where

$$\begin{aligned}
a_1 &= -\left(\sigma\beta I^* + (1-\sigma)\lambda I^* + \alpha + \mu_1\right),\\
a_2 &= -\left(\sigma\beta S^* + (1-\sigma)\lambda S^*\right),\\
a_3 &= \left(\sigma\beta I^* + (1-\sigma)\lambda I^*\right),\\
a_4 &= -\gamma - \mu_2,\ a_5 = \sigma\beta S^* + (1-\sigma)\lambda S^*,\\
a_6 &= -\left(\theta+\eta+\mu_3\right),\ b_1 = -\delta,\ b_2 = \delta.
\end{aligned}$$

The characteristic equation of the linearized system (4) is

$$\mu^3 + c_1\mu^2 + c_2\mu + c_3 + e^{-\mu\tau}\left(d_1\mu^2 + d_2\mu + d_3\right) = 0, \tag{5}$$

where

$$\begin{aligned}
c_1 &= -(a_1 + a_4 + a_5 + a_6),\\
c_2 &= (a_1a_4 + a_1a_5 + a_1a_6 + a_4a_6 + a_1a_6),\\
c_3 &= -a_1a_6(a_4 + a_5),\\
d_1 &= -b_1,\\
d_2 &= (a_1 + a_6)b_1,\\
d_3 &= -(a_1a_6b_1 + a_2a_3b_2).
\end{aligned}$$

For $\tau = 0$, equation (5) reduces to $\mu^3+\rho_1\mu^2+\rho_2\mu+\rho_3 = 0$, where $\rho_1 = c_1 + d_1$, $\rho_2 = c_2 + d_2$, $\rho_3 = c_3 + d_3$. If the condition

$$H_1 : \rho_1 > 0, \rho_3 > 0 \text{ and } \rho_1\rho_2 - \rho_3 > 0$$

is satisfied, then system (3) is locally asymptotically stable when $\tau = 0$.

Next, we consider the time delay τ as a parameter to analyze the local stability of the equilibrium $P^*(S^*, E^*, I^*, R^*)$ and explore the occurrence of a Hopf bifurcation in the system described by (3). For $\tau > 0$, suppose that $\mu = i\omega$ $(\omega > 0)$ is a root of (5). Then

$$(i\omega)^3 + c_1(i\omega)^2 + c_2(i\omega) + c_3 + e^{-i\omega\tau}\left[d_1(i\omega)^2 + d_2(i\omega) + d_3\right] = 0. \quad (6)$$

Separating the real and imaginary parts in (6), we get

$$\left(d_3 - d_1\omega^2\right)\cos\omega\tau + d_2\omega\sin\omega\tau = c_1\omega^2 - c_3, \quad (7)$$

$$d_2\omega\cos\omega\tau - \left(d_3 - d_1\omega^2\right)\sin\omega\tau = \omega^3 - c_2\omega, \quad (8)$$

which leads to

$$\omega^6 + \kappa_1\omega^4 + \kappa_2\omega^2 + \kappa_3 = 0, \quad (9)$$

where

$$\kappa_1 = c_1^2 - 2c_2 - d_1^2,$$
$$\kappa_2 = c_2^2 - 2c_1c_3 + 2d_1d_3 - d_2^2,$$
$$\kappa_3 = c_3^2 - d_3^2.$$

Let $\omega^2 = \varsigma$. Then equation (9) takes the form

$$\varsigma^3 + \kappa_1\varsigma^2 + \kappa_2\varsigma + \kappa_3 = 0. \quad (10)$$

Based on the above analysis, we introduce the following assumption to establish the main results presented in this paper.

H_2 : If equation (10) has at least one positive root, then there exists a positive root ζ_0 of (10) such that equation (5) possesses a pair of purely imaginary roots $\pm i\zeta_0$.

For $\omega_0^2 = \zeta_0$, the corresponding critical value τ_0 is

$$\tau_0 = \frac{1}{\varsigma_0}\cos^{-1}\left[\frac{\omega_0^4(d_2 - d_1c_1)}{\left(d_3 - d_1\omega_0^2\right)^2 + d_2^2\omega_0^2} + \frac{\omega_0^2(d_1c_3 - d_2c_2 + d_3c_1) - d_3c_3}{\left(d_3 - d_1\omega_0^2\right)^2 + d_2^2\omega_0^2}\right].$$

In the following, we will show that the transversality condition of Hopf bifurcation is also satisfied. Differentiating (5) on τ and applying the implicit function theorem, we obtain

$$\left(\frac{d\lambda}{d\tau}\right)^{-1} = -\frac{3\lambda^2 + 2\lambda c_1 + c_2}{\lambda\left(\lambda^3 + c_1\lambda^2 + c_2\lambda + c_3\right)} + \frac{2\lambda d_1 + d_2}{\lambda\left(d_1\lambda^2 + d_2\lambda + d_3\right)} - \frac{\tau}{\lambda}.$$

Hence, we get

$$\mathrm{Re}\left(\frac{d\lambda}{d\tau}\right)^{-1}_{\tau=\tau_0} = \frac{y(\varsigma_0)}{\left(d_3 - d_1\omega_0^2\right)^2 + d_2^2\omega_0^2},$$

where $y(\varsigma_0) = \varsigma^3 + \kappa_1\varsigma^2 + \kappa_2\varsigma + \kappa_3 = 0$. It is evident that if the condition

$$H_3 : y(\varsigma_0) \neq 0$$

holds, then $\mathrm{Re}\left[d\lambda/d\tau\right]^{-1}_{\tau=\tau_0} \neq 0$. According to the Hopf bifurcation theorem in [29], we derive the following results for the system (3).

Theorem 1: If conditions H_1-H_3 are satisfied, then the positive equilibrium $P^*(S^*, E^*, I^*)$ of system (3) is locally asymptotically stable for $\tau \in [0, \tau_0)$. Furthermore, system (3) undergoes a Hopf bifurcation at $P^*(S^*, E^*, I^*)$ when $\tau = \tau_0$, leading to the emergence of a family of periodic solutions bifurcating from the positive equilibrium $P^*(S^*, E^*, I^*)$ near $\tau = \tau_0$.

III. DIRECTION AND STABILITY OF Hopf BIFURCATION

In the preceding section, we demonstrated that system (3) displays a set of periodic solutions emerging from the positive equilibrium $P^*(S^*, E^*, I^*)$. By applying the normal form theory and the center manifold theorem introduced by Hassard et al. [30], we will now derive a precise formula for determining the direction and stability of the Hopf bifurcation at these critical values. Define

$$u_1 = S(t) - S^*,\ u_2 = E(t) - E^*,\ u_3 = I(t) - I^*,$$

and rescale the delay $t \to t/\tau$. Let $\tau = \tau_0 + \mu$, where $\mu = 0$ represents the Hopf bifurcation value of (3). Then, system (3) can be reformulated as a functional differential equation in $C = C\left([-1, 0], \mathbb{R}^3\right)$ as follows

$$\dot{u}_t = L_\mu(u_t) + F(\mu, u_t), \quad (11)$$

where $u(t) = (u_1, u_2, u_3)^T \in C = C\left([-1, 0], \mathbb{R}^3\right)$, and the functions $L_\mu : C \to \mathbb{R}^3$, $F : \mathbb{R} \times C \to \mathbb{R}^3$ given by

$$L_\mu(\psi) = (\tau_0 + \mu)\left[N_{\max}\psi(0) + Z_{\max}\psi(-1)\right], \quad (12)$$

$$F(\mu, \Phi) = (\tau_0 + \mu) \cdot \begin{bmatrix} -\Phi_1(0)\Phi_3(0)(\sigma\beta + (1-\sigma)\lambda) \\ \Phi_1(0)\Phi_3(0)(\sigma\beta + (1-\sigma)\lambda) \\ 0 \end{bmatrix}, \quad (13)$$

where

$$N = \begin{bmatrix} a_1 & 0 & a_2 \\ a_3 & a_4 & a_5 \\ 0 & 0 & a_6 \end{bmatrix},\ Z = \begin{bmatrix} 0 & 0 & 0 \\ 0 & b_1 & 0 \\ 0 & b_2 & 0 \end{bmatrix}.$$

By the Riesz-Representation theorem, we can find a function $\omega(\varsigma, \mu)$ of bounded variation such that

$$L_\mu(\vartheta) = \int_{-1}^{0} d\omega(\varsigma, \mu)\vartheta(\varsigma), \text{ for } \vartheta \in C, \quad (14)$$

We may take

$$\omega(\varsigma, \mu) = (\tau_0 + \mu)\left[N_{\max}\chi(\theta) + Z_{\max}\cdot\chi(\theta + 1)\right], \quad (15)$$

where $\chi(\theta)$ is the Dirac-Delta function.

For $\vartheta \in C^1\left([-1,0],\mathbb{R}^3\right)$, let

$$M(\mu)\vartheta(\omega)=\begin{cases}\dfrac{d\vartheta}{d\theta}, & -1\le\varsigma<0,\\ \displaystyle\int_{-1}^{0} d\omega(s,\mu)\vartheta(s,\zeta)=0 & \varsigma=0,\end{cases}$$

and

$$\Delta(\mu)\vartheta(\varsigma)=\begin{cases}0, & -1\le\varsigma<0,\\ F(\mu,\vartheta), & \varsigma=0.\end{cases}$$

Then, system (11) is equivalent to

$$\dot{u}_t=M(\mu)u_t+\Delta(\mu)u_t, \tag{16}$$

where $u_t=u(t+\varsigma)$ for $\varsigma\in[-1,0]$.

For $\psi\in C^1\left([0,1],\left(\mathbb{R}^3\right)^*\right)$, define

$$M^*(\mu)\psi(s)=\begin{cases}-\dfrac{d\psi(s)}{ds}, & 0<s\le 1,\\ \displaystyle\int_{-1}^{0} d\omega^T(t,0)\psi(-t), & s=0,\end{cases}$$

and a bilinear inner product

$$<\psi(s),\vartheta(\varsigma)>=\bar{\psi}(0)\vartheta(0)-\int_{\zeta=-1}^{0}\int_{\xi=0}^{\varsigma}\bar{\psi}(\xi-\zeta)d\omega(\zeta)\vartheta(\xi)d\xi, \tag{17}$$

where $\omega(\varsigma)=\omega(\varsigma,0)$. Let $\Im(t)=(1,\Im_2,\Im_3)^T e^{i\omega_0\tau_0\varsigma}$ and $\Im^*(s)=Q\left(1,\Im_2^*,\Im_3\right)^T e^{i\omega_0\tau_0 s}$ be the eigenvectors of $M(0)$ and $M^*(0)$ respectively, which correspond to $i\omega_0\tau_0$ and $-i\omega_0\tau_0$. One has

$$\Im_2=\frac{i\omega_0-a_1}{a_2},\quad \Im_3=\frac{a_3+a_5\Im_2}{i\omega_0-a_4-b_1e^{-i\omega_0\tau_0}},$$
$$\Im_2^*=-\frac{a_1+i\omega_0}{a_3},\quad \Im_3^*=-\frac{a_2+a_5\Im_2^*}{a_6+i\omega_0}.$$

According to equation (17), we have the following.

$$\bar{Q}=\left[1+\Im_2\bar{\Im}_2^*+\Im_3\bar{\Im}_3^*+\tau e^{-i\tau_0\omega_0^*}\left(b_1\Im_2+b_2\Im_3\right)\right]^{-1},$$

such that $\langle\Im^*,\Im\rangle=1$ and $\left\langle\Im^*,\bar{\Im}\right\rangle=0$. Next, we derive expressions for A_{20},A_{11},A_{02} and A_{21} using the algorithms presented in [31] and the computational process described in [32]. Throughout the rest of this section, we adopt the same notions as those used by Rezapour et al. [33] and Wei et al. [34]. Initially, we compute the coordinates necessary to describe the center manifold c_0 at $\mu=0$. Let u_t be the solution of (16) when $\mu=0$. Define

$$\Gamma(t)=\left\langle\zeta^*,u_t\right\rangle,\ K(t,\theta)=u_t(\theta)-2\mathrm{Re}\{\Gamma(t)\Omega(\varsigma)\}.$$

On the center manifold c_0,

$$K(t,\theta)=K(\Gamma(t),\bar{\Gamma}(t),\zeta)K(\Gamma,\bar{\Gamma})=K_{02}\frac{\Gamma^2}{2}+K_{11}\Gamma\bar{\Gamma}+K_{02}\frac{\bar{\Gamma}^2}{2}+\cdots, \tag{18}$$

where Γ and $\bar{\Gamma}$ are local coordinates for center manifold c_0 in the direction of ζ^* and $\bar{\zeta}^*$. Now,

$$\begin{aligned}\dot{\Gamma}(t)&=\left\langle\zeta^*,u_t\right\rangle\\&=\left\langle Z^*(0)\zeta^*,u_t\right\rangle+\bar{\zeta}^*(0)\Delta(0)u_t\\&\quad-\int_{-1}^{0}\int_{0}^{\zeta}\bar{\zeta}^*(\xi-\zeta)d\omega(\zeta)Z(0)\Delta(0)u_t(\xi)d\xi\\&=i\omega_0\tau_0\Gamma(t)+\bar{\zeta}^*(0)f\ (0,unto(\theta))\\&=I\omega_0\tau_0\Gamma(t)+\bar{\zeta}^*(0)f_0(\Gamma(t),\widehat{\Gamma}(t)),\end{aligned}$$

which can be reformulated as

$$\dot{\Gamma}=I\omega_0\tau_0\Gamma(t)+A(\Gamma,\widehat{\Gamma}), \tag{19}$$

where

$$A(\Gamma,\bar{\Gamma})=A_{20}\frac{\Gamma^2}{2}+A_{11}\Gamma\bar{\Gamma}+A_{02}\frac{\bar{\Gamma}^2}{2}+A_{21}\frac{\Gamma^2\bar{\Gamma}}{2}+\cdots. \tag{20}$$

As a result, we get

$$\begin{aligned}A(\Gamma,\bar{\Gamma})&=\bar{\zeta}^*(0)\cdots f_0(\Gamma,\bar{\Gamma})\\&=\overline{B}\left(1,\bar{\Im}_2^*,\bar{\Im}_3^*\right)\left(f_1\left(0,u_t\right),f_2\left(0,u_t\right),0\right)^T,\end{aligned} \tag{21}$$

where

$$\begin{aligned}f_1\left(0,u_t\right)&=-(\sigma\beta+(1-\sigma)\lambda)\tau_0\Phi_1(0)\Phi_3(0),\\f_2\left(0,u_t\right)&=(\sigma\beta+(1-\sigma)\lambda)\tau_0\Phi_1(0)\Phi_3(0).\end{aligned} \tag{22}$$

Since

$$\begin{aligned}u_t=u(t+\theta)&=K(\Gamma,\bar{\Gamma},\zeta)+\Gamma\Omega(\zeta)+\bar{\Gamma}\Omega(\zeta),\\\Omega(\zeta)&=(1,\Im_2,\Im_3)^T e^{i\omega_0\tau_\zeta\zeta},\end{aligned} \tag{23}$$

we have

$$u_t=\begin{bmatrix}u_1(t+\theta)\\u_2(t+\theta)\\0\end{bmatrix}+\begin{bmatrix}K^{(1)}(t+\theta)\\K^{(2)}(t+\theta)\\0\end{bmatrix}+\Gamma\begin{bmatrix}1\\\Omega_2\\\Omega_3\end{bmatrix}e^{i\omega_0\tau_0\zeta}+\bar{\Gamma}\begin{bmatrix}1\\\bar{\Omega}_2\\\bar{\Omega}_3\end{bmatrix}e^{-i\omega_0\tau_0\zeta}, \tag{24}$$

and

$$\Phi_1(0) = \Gamma + \bar{\Gamma} + K_{20}^{(1)}(0)\cdot\frac{\Gamma^2}{2} + K_{11}^{(1)}(0)\cdot\Gamma\bar{\Gamma} + K_{02}^{(1)}(0)\cdot\frac{\bar{\Gamma}^2}{2} + \cdots,$$

$$\Phi_2(0) = \Gamma\Omega_2 + \bar{\Gamma}\bar{\Omega}_2 + K_{20}^{(2)}(0)\cdot\frac{\Gamma^2}{2} + K_{11}^{(2)}(0)\cdot\Gamma\bar{\Gamma} + K_{02}^{(1)}(0)\cdot\frac{\bar{\Gamma}^2}{2} + \cdots,$$

$$\Phi_3(0) = \Gamma\Omega_3 + \bar{\Gamma}\bar{\Omega}_3 + K_{20}^{(3)}(0)\cdot\frac{\Gamma^2}{2} + K_{11}^{(3)}(0)\cdot\Gamma\bar{\Gamma} + K_{02}^{(3)}(0)\cdot\frac{\bar{\Gamma}^2}{2} + \cdots.$$

From (20) and (21), it follows

$$A(\Gamma,\bar{\Gamma}) = \overline{B}\left(1,\bar{\Omega}_2^*,\bar{\Omega}_3^*\right)\cdot\begin{bmatrix} P_{11}\Gamma^2 + P_{12}\Gamma\bar{\Gamma} + P_{13}\bar{\Gamma}^2 + P_{14}\Gamma^2\bar{\Gamma} \\ P_{21}\Gamma^2 + P_{22}\Gamma\bar{\Gamma} + P_{23}\bar{\Gamma}^2 + P_{24}\Gamma^2\bar{\Gamma} \\ 0 \end{bmatrix} + \cdots, \tag{25}$$

where

$$P_{11} = -[\sigma\beta + (1-\sigma)\lambda]\tau_0\left(\Omega_2+\Omega_3\right),$$
$$P_{12} = -[\sigma\beta + (1-\sigma)\lambda]\tau_0\left(\Omega_2+\bar{\Omega}_2+\Omega_3+\bar{\Omega}_3\right),$$
$$P_{13} = -[\sigma\beta + (1-\sigma)\lambda]\tau_0\left(\bar{\Omega}_2+\bar{\Omega}_3\right),$$
$$P_{14} = -[\sigma\beta + (1-\sigma)\lambda]\tau_0,$$
$$P_{21} = [\sigma\beta + (1-\sigma)\lambda]\tau_0\left(\Omega_2+\Omega_3\right),$$
$$P_{22} = [\sigma\beta + (1-\sigma)\lambda]\tau_0\left(\Omega_2+\bar{\Omega}_2+\Omega_3+\bar{\Omega}_3\right),$$
$$P_{23} = [\sigma\beta + (1-\sigma)\lambda]\tau_0\left(\bar{\Omega}_2+\bar{\Omega}_3\right),$$
$$P_{24} = [\sigma\beta + (1-\sigma)\lambda]\tau_0.$$

Thus,

$$A(\Gamma,\bar{\Gamma}) = \overline{B}\left[\left(P_{11}+\bar{\Omega}_2^*P_{21}\right) + \left(P_{12}+\bar{\Omega}_2^*P_{22}\right)\Gamma\bar{\Gamma} + \left(P_{13}+\bar{\Omega}_2^*P_{23}\right)\bar{\Gamma}^2 + \left(P_{14}+\bar{\Omega}_2^*P_{24}\right)\Gamma^2\bar{\Gamma}\right] + \cdots. \tag{26}$$

Comparing the coefficients in (25) with those in (20), we can get,

$$\mathrm{A}_{20} = 2\,\overline{\mathrm{B}}\left(\mathrm{P}_{11}+\bar{\Omega}_2^*\mathrm{P}_{21}\right),\ \mathrm{A}_{11} = \overline{\mathrm{B}}\left(\mathrm{P}_{12}+\bar{\Omega}_2^*\mathrm{P}_{22}\right),$$
$$\mathrm{A}_{02} = 2\,\overline{\mathrm{B}}\left(\mathrm{P}_{13}+\bar{\Omega}_2^*\mathrm{P}_{23}\right),\ \mathrm{A}_{21} = 2\,\overline{\mathrm{B}}\left(\mathrm{P}_{14}+\bar{\Omega}_2^*\mathrm{P}_{24}\right).$$

To derive the expression for A_{21}, we first need to calculate $K_{11}(\varsigma)$ and $K_{20}(\varsigma)$. Using (11) and (18), we find

$$\dot{K} = \begin{cases} ZK - 2\mathrm{Re}\{\bar{\Omega}(0)\cdot f\Omega\{\zeta\}\},\ -1\le\zeta<0, \\ ZK - 2\mathrm{Re}\{\bar{\Omega}(0)\cdot f\Omega\{\zeta\}\} + f,\ \zeta=0. \end{cases} \tag{27}$$

Define (26) as

$$\dot{K} = ZK + H(\Gamma,\bar{\Gamma},\zeta), \tag{28}$$

where

$$H(\Gamma,\bar{\Gamma},\zeta) = H_{20}(\zeta)\frac{\Gamma^2}{2} + H_{11}(\zeta)\frac{\Gamma\bar{\Gamma}}{2} + H_{02}(\zeta)\frac{\bar{\Gamma}^2}{2} + \cdots. \tag{29}$$

From (18),(19),(28) and (29), we obtain the following relations

$$(2i\omega_0\tau_0 - Z)\,K_{20}(\zeta) = H_{20}(\zeta), \tag{30}$$

$$ZK_{11}(\zeta) = -H_{11}(\zeta). \tag{31}$$

Additionally, (20) and (27) give

$$\begin{aligned} H(\Gamma,\bar{\Gamma},\zeta) &= -2\mathrm{Re}\left\{\bar{\Omega}^*(0)f_0\Omega(\zeta)\right\} \\ &= -2\mathrm{Re}\{A(\Gamma,\bar{\Gamma})\Omega(\zeta)\} \\ &= -(\Gamma,\bar{\Gamma})\Omega(\zeta) - \overline{A}(\Gamma,\bar{\Gamma})\bar{\Omega}(\zeta) \\ &= -\left[A_{02}\frac{\Gamma^2}{2} + A_{11}\Gamma\bar{\Gamma} + A_{02}\frac{\bar{\Gamma}^2}{2} + A_{21}\frac{\Gamma^2\bar{\Gamma}}{2}\right]\Omega(\zeta) \\ &\quad - \left[\overline{A}_{02}\frac{\bar{\Gamma}^2}{2} + \overline{A}_{11}\Gamma\bar{\Gamma} + \overline{A}_{02}\frac{\bar{\Gamma}^2}{2} + \overline{A}_{21}\frac{\Gamma\bar{\Gamma}^2}{2}\right]\bar{\Omega}(\zeta). \end{aligned} \tag{32}$$

By comparing the coefficients in (29) and (32), we arrive at

$$H_{20}(\zeta) = -A_{20}\Omega(\zeta) - \overline{A}_{02}\bar{\Omega}(\zeta), \tag{33}$$

$$H_{11}(\zeta) = -A_{11}\Omega(\zeta) - \overline{A}_{11}\bar{\Omega}(\zeta), \tag{34}$$

where $\zeta\in[-1,0)$. From (30),(33) and the definition of $Z(0)$, we have

$$K_{20}(\zeta) = 2i\omega_0\tau_0K_{20}(\zeta) + A_{20}\Omega(\zeta) + \overline{A}_{02}\bar{\Omega}(\zeta). \tag{35}$$

According to $\Omega(\zeta) = \Omega(0)e^{i\omega_0\tau_0}$, we get

$$K_{20}(\zeta) = \frac{iA_{20}}{\omega_0\tau_0}\Omega(0)e^{i\omega_0\tau_0} + \frac{\bar{i}\overline{A}_{02}}{3\omega_0\tau_0}\bar{\Omega}(0)e^{-i\omega_0\tau_0} + \Theta_1e^{2i\omega_0\tau_0}, \tag{36}$$

and, similarly,

$$K_{11}(\zeta) = -\frac{iA_{11}}{\omega_0\tau_0}\Omega(0)e^{i\omega_0\tau_0} + \frac{\bar{i}\overline{A}_{11}}{\omega_0\tau_0}\bar{\Omega}(0)e^{-i\omega_0\tau_0} + \Theta_2, \tag{37}$$

where Θ_1 and Θ_2 are both constant vectors. In the subsequent analysis, we will determine Θ_1 and Θ_2. From the definition of $Z(0)$, along with (33) and (34), it follows

$$\int_{-1}^{0} d\omega(\zeta)K_{20}(\zeta) = 2i\omega_0\tau_0\,K_{20}(\zeta) - H_{20}(\zeta), \tag{38}$$

$$\int_{-1}^{0} d\omega(\zeta)K_{11}(\zeta) = -H_{11}(0). \tag{39}$$

From (30) and (31)

$$H_{20}(0) = -A_{20}\Omega(\zeta) - \bar{A}_{02}\bar{\Omega}(\zeta) + (P_{11}, P_{21}, 0)^T, \quad (40)$$

$$H_{11}(\zeta) = -A_{11}\Omega(\zeta) - \bar{A}_{11}\bar{\Omega}(\zeta) + (P_{12}, P_{22}, 0)^T. \quad (41)$$

Notice that

$$\left[i\omega_0\tau_0 I - \int_{-1}^{0} d\omega(\zeta)e^{i\omega_0\tau_0}\right]\Omega(0) = 0,$$
$$\left[-i\omega_0\tau_0 I - \int_{-1}^{0} d\omega(\zeta)e^{-i\omega_0\tau_0}\right]\bar{\Omega}(0) = 0. \quad (42)$$

Substituting (36) and (40) into (38), we obtain

$$\left[2i\omega_0\tau_0 I - \int_{-1}^{0} d\omega(\zeta)e^{2i\omega_0\tau_0}\right]\Theta_1 = \begin{bmatrix} P_{11} \\ P_{21} \\ 0 \end{bmatrix}, \quad (43)$$

i.e.

$$\left[2i\omega_0\tau_0 I - N - Ze^{-2i\omega_0\tau_0}\right]\Theta_1 = \begin{bmatrix} P_{11} \\ P_{21} \\ 0 \end{bmatrix}. \quad (44)$$

Thus, we have

$$\Theta_1 = \frac{2}{\tau_0}\begin{bmatrix} a_1^1 & 0 & a_2^1 \\ -a_3^1 & a_4^1 & -a_5^1 \\ 0 & 0 & a_6^1 \end{bmatrix}^{-1}\begin{bmatrix} P_{11} \\ P_{21} \\ 0 \end{bmatrix},$$

where

$$a_1^1 = 2i\omega_0 - a_1,\ a_2^1 = 2i\omega_0 - a_2,$$
$$a_3^1 = 2i\omega_0 - a_3,\ a_4^1 = -a_4 - b_1e^{-2i\omega_0\tau_0},$$
$$a_5^1 = 2i\omega_0 - a_5,\ a_6^1 = 2i\omega_0 - a_6.$$

Similarly, we have

$$\int_{-1}^{0} d\omega(\zeta)\Theta_2 = \begin{bmatrix} P_{12} \\ P_{22} \\ 0 \end{bmatrix}. \quad (45)$$

On the other hand,

$$(N + Z)F_2 = \begin{bmatrix} p_{12} \\ p_{22} \\ 0 \end{bmatrix}, \quad (46)$$

so that

$$F_2 = \frac{1}{\tau_0}\begin{bmatrix} a_1 & 0 & a_2 \\ a_3 & b_1^1 & a_5 \\ 0 & b_2^1 & a_6 \end{bmatrix} \times \begin{bmatrix} p_{12} \\ p_{22} \\ 0 \end{bmatrix}, \quad (47)$$

where

$$b_1^1 = a_4 + b_1,\ b_2^1 = b_1. \quad (48)$$

In conclusion, we can compute the following values

$$\Omega_1(0) = \frac{i}{2\omega_0\tau_0}\left[A_{11}A_{20} - 2|A_{11}|^2 - \frac{|A_{02}|^2}{2}\right],$$
$$\mu_2 = -\frac{\mathrm{Re}\{\Omega_1(0)\}}{\mathrm{Re}\{\mu'(\tau_0)\}},$$
$$\beta_2 = 2\mathrm{Re}\{\Omega_1(0)\},$$
$$T_2 = \frac{-\mathrm{Im}\{\Omega_1(0)\} + \mu_2\mathrm{Im}\{\mu'(\tau_0)\}}{\omega_0\tau_0},$$

which are fundamental for understanding the dynamics of the system near the bifurcation point. Now, the main results of this section are summarized as follows.

Theorem 2: 1) μ_2 determines the direction of the Hopf bifurcation. If $\mu_2 > 0$, the Hopf bifurcation is supercritical, whereas if $\mu_2 < 0$ it is subcritical.

2) β_2 determines the stability of the bifurcating periodic solutions. If $\beta_2 < 0$, the solutions are stable, while if $\beta_2 > 0$ they are unstable.

3) T_2 determines the change in the period of the bifurcating periodic solutions. If $T_2 > 0$, the period increases, while if $T_2 < 0$, the period decreases.

IV. ESTIMATION OF DELAY DURATION

In this section, we analyze the stability of periodic bifurcation oscillations and determine the necessary delay duration required to maintain the stability of the periodic limit cycle. The system (3) is defined by continuous real-valued functions over $[-\tau, +\infty)$, with initial conditions specified for the interval $[-\tau, 0)$. By linearizing (3) at the coexisting equilibrium point associated with the propagation of the worm, we derive

$$\begin{aligned}\dot{S} &= [\sigma\beta + (1-\sigma)\lambda]\left(SI^* + S^*I\right) - \alpha S - \mu_1 S,\\ \dot{E} &= [\sigma\beta + (1-\sigma)\lambda]\left(SI^* + S^*I\right) - \delta E(t-\tau)\\ &\quad - \gamma E - \mu_2 E,\\ \dot{I} &= \delta E(t-\tau) - \theta I - \eta I - \mu_3 I. \end{aligned} \quad (49)$$

Applying the Laplace transform to (49) results in

$$\begin{aligned}&L_s(\rho)\left\{\rho + \alpha + \mu_1 + [\sigma\beta + (1-\sigma)\lambda]I^*\right\}\\ &= -[\sigma\beta + (1-\sigma)\lambda]S^*L_I(\rho) + S(0),\\ &L_E(\rho)[\rho + \gamma + \mu_2] = [\sigma\beta + (1-\sigma)\lambda]I^*L_s(\rho)\\ &\quad + [\sigma\beta + (1-\sigma)\lambda]S^*L_I(\rho)\\ &\quad - \delta e^{-\rho\tau}[L_I(\rho) + K_E(\rho)] + E(0),\\ &L_I(\rho)[\rho + (\theta + \eta + \mu_3)] = \delta e^{-\rho\tau}[L_E(\rho) + K_E(\rho)] + I(0),\end{aligned}$$

where

$$K_E(\rho) = \int_{-\tau}^{0} e^{-\rho\tau}E(t)dt,\ K_I(\rho) = \int_{-\tau}^{0} e^{-\rho\tau}I(t)dt,$$

with $L_S(\rho)$, $L_E(e)$, and $L_I(\rho)$ being the Laplace transforms of $S(t)$, $E(t)$, and $I(t)$, respectively.

Based on the results of Freedman et al. [35] and the Nyquist criteria [36], the conditions for local asymptotic stability of P^* are

$$\mathrm{Im}\left[M\left(i\rho_0\right)\right] > 0, \tag{50}$$

$$\mathrm{Re}\left[M\left(i\rho_0\right)\right] > 0, \tag{51}$$

$$M(\rho) = \left(\rho^3 + c_1\rho^2 + c_2\rho + c_3\right) + e^{-\rho\tau}\left(d_1\rho^2 + d_2\rho + d_3\right) = 0, \tag{52}$$

where ρ_0 is the smallest non-negative root of (51). We have determined that P^* remains stable in the absence of time delay ($\tau = 0$). Equations (50) and (51) can be written explicitly as

$$-\rho_0^3 + c_2\rho_0 > \left(d_3 - d_1\rho_0^2\right)\sin\left(\rho_0\tau\right) - d_2\rho_0\cos\left(\rho_0\tau\right), \tag{53}$$

$$-c_1\rho_0^2 + c_3 = -d_2\rho_0\sin\left(\rho_0\tau\right) - \left(d_3 - d_1\rho_0^2\right)\cos\left(\rho_0\tau\right). \tag{54}$$

These conditions allow us to estimate the duration of the time delay τ sufficient for the stability of the steady state P^*. Our goal is to identify the maximum limit ρ_+ for ρ_0 that remains unaffected by the time delay τ_+, and to calculate the corresponding duration of τ. Consequently, equation (53) remains valid for all values of ρ within the range $0 \le e \le e_+$ at $e = e_0$. We rewrite (54) as

$$a_1\rho_0^2 = a_3 + d_3\cos\left(\rho_0\tau\right) + d_2\rho_0\sin\left(\rho_0\tau\right) - d_1\rho_0^2\cos\left(\rho_0\tau\right). \tag{55}$$

Maximizing the right side of (55) leads to

$$d_3\cos\left(\rho_0\tau\right) + d_2\rho_0\sin\left(\rho_0\tau\right) - d_1\rho_0^2\cos\left(\rho_0\tau\right), \tag{56}$$

subject to

$$\left|\cos\left(\rho_0\tau\right)\right| \le 1, \qquad \left|\sin\left(\rho_0\tau\right)\right| \le 1.$$

Therefore, it follows from (56) that

$$\left|a_1\right|\rho_0^2 \le \left|a_3\right| + \left|d_3\right| + \left|d_2\right|\rho_0 + \left|d_1\right|\rho_0^2,$$

which can be expressed as

$$\left(\left|a_1\right| - \left|d_1\right|\right)e_0^2 - \left|d_2\right|e_0 - \left(\left|a_3\right| - \left|d_3\right|\right) \le 0.$$

From this inequality, we get

$$\rho_+ \le \frac{1}{2\left(\left|a_1\right| - \left|d_1\right|\right)} \cdot \left[\left|d_2\right| + \sqrt{\left|d_2\right|^2 + 4\left(\left|a_1\right| - \left|d_1\right|\right)\left(\left|a_3\right| - \left|d_3\right|\right)}\right]. \tag{57}$$

It is obvious from (57) that $\rho_0 \le \rho_+$. Also, from the inequality (53), we have

$$\rho_0^2 < a_2 + d_2\cos\left(\rho_0\tau\right) + d_1\rho_0\sin\left(\rho_0\tau\right)\frac{-d_3\sin\left(\rho_0\tau\right)}{\rho_0}.$$

Since P^* is asymptotically stable without time lag for sufficiently small $\tau > 0$, the inequality (57) is satisfied. Substituting (55) into (57) and rearranging terms leads to

$$\left(d_3 - d_1\rho_0^2 - a_1d_2\right)\left[\cos\left(\rho_0\tau\right) - 1\right] + \left[\left(d_2 - a_1d_1\right)\rho_0 + \frac{a_1d_3}{e_0}\right]\sin\left(\rho_0\tau\right) < a_1a_2 - a_3 - d_3 + d_1\rho_0^2 + a_1d_2. \tag{58}$$

Using bounds, we find

$$\left(d_3 - d_1\rho_0^2 - a_1d_2\right)\left[\cos\left(\rho_0\tau\right) - 1\right] = 2\left[d_1\rho_0^2 + a_1d_2 - d_3\right]\sin^2\left(\frac{\rho_0\tau}{2}\right) \le \frac{1}{2}\left|\left(d_1\rho_+^2 + a_1d_2 - d_3\right)\right|\rho_+^2\tau^2$$

and

$$\left[\left(d_2 - a_1d_1\right)\rho_0 + \frac{a_1d_3}{\rho_0}\right]\sin\left(\rho_0\tau\right) \le \left(\left|d_2 - a_1d_1\right|\rho_+^2 + \left|a_1\right|\left|d_3\right|\right)\tau.$$

By simplifying (58), we arrive at

$$\Pi_1\tau_1^2 + \Pi_2\tau_2^2 + \Pi_3\tau_3^2,$$

where

$$\Pi_1 = \frac{1}{2}\left|\left(d_1\rho_+^2 + a_1d_2 - d_3\right)\right|\rho_+^2,$$

$$\Pi_2 = \left|\left(d_2 - a_1d_1\right)\rho_+^2 + \left|a_1\right|\right|d_3||,$$

$$\Pi_3 = \left|\left(d_2 - a_1d_1\right)\rho_+^2 + \left|a_1\right|\right|d_3||.$$

Finally, solving for τ, we have

$$\tau_+ = \frac{1}{2\Pi_1}\left[-\Pi_2 + \sqrt{\Pi_2^2 + 4\Pi_1\Pi_3}\right],$$

for $0 \le \tau \le \tau_+$, This guarantees that the Nyquist conditions are met and provides an estimate τ_+ for the maximum allowable delay needed to maintain the stability of the limit cycle.

V. OPTIMAL CONTROL OF WORM PROPAGATION

We now implement optimal control strategies through vaccination and treatment to minimize the number of infected individuals in the HIoT system while ensuring minimal investment in resources to control the spread of worms [37], [38], [39]. This issue is modeled as an optimization problem for a vaccination and treatment strategy involving two control variables V_c, T_c. Presently, we employ two doses to represent the proportion of exposed and infected individuals who are vaccinated and treated, respectively, at a given time.

Consequently, (2) evolves as follows

$$\begin{aligned}
\dot{S} &= \Pi - (1 - V_c)\,\sigma\beta SI - (1 - T_c)\,(1 - \sigma)\lambda SI \\
&\quad - \alpha S - \mu_1 S, \\
\dot{E} &= (1 - V_c)\,\sigma\beta SI + (1 - T_c)\,(1 - \sigma)\lambda SI \\
&\quad - \delta E(t - \tau) - \gamma E - \mu_2 E - V_c E, \\
\dot{I} &= \delta E(t - \tau) - \theta I - \eta I - \mu_3 I - T_c I, \\
\dot{R} &= \alpha S + \gamma E + \theta I - \mu_4 R + V_c E + T_c I,
\end{aligned} \tag{59}$$

$$S(0) = S_0,\ E(0) = E_0,\ I(0) = I_0,\ R(0) = R_0. \tag{60}$$

It can be shown that for the system (59) there is a unique solution $(S(t), E(t), I(t), R(t))$ with initial data (S_0, E_0, I_0, R_0). The objective is to minimize the cost associated with providing functional control measures

$$\begin{aligned}
\Im\,(V_c, T_c) = \int_0^{t_f} \Big[& Z_1 E(t) + Z_2 I(t) + \frac{1}{2} A_1 V_c^2(t) \\
& + \frac{1}{2} A_2 T_c^2(t) \Big]\, dt.
\end{aligned} \tag{61}$$

In other words, the control variables $(V_c, T_c) \in VT_{ad}$ represent the percentage of exposed and infected individuals being vaccinated and treated respectively, per unit of time, and VT_{ad} is the admissible control set. In the differential equation system (59), the cost function is designed to minimize the impact of the exposed population $E(t)$ and the infected population $I(t)$, as represented by the first two terms. The parameters Z_1 and Z_2 are positive constants that maintain equilibrium in sizes of $E(t)$ and $I(t)$, respectively. Additionally, the second term in the cost function introduces quadratic terms $A_1 V_c^2(t)/2$ and $A_2 T_c^2(t)/2$, where $A_1,\ A_2$ are positive weighting parameters associated with the controls V_c and T_c. These quadratic terms reflect the severity of the side effects caused by vaccination and treatment. The objective is to minimize the administrative costs defined in (61) by reducing the number of exposed and infected nodes while employing minimally probable control variables (V_c, T_c). Here, the control variables $(V_c, T_c) \in VT_{ad}$ represent the proportion of exposed and infected individuals vaccinated and treated at any given time. The admissible control set is defined as

$$\begin{aligned}
VT_{ad} = \{ & VT = (V_c, T_c) : V_c, T_c \text{measurable}, \\
& 0 \le V_c, T_c \le VT^{\max} \le 1, t \in [0, t_f] \},
\end{aligned}$$

where $V^{\max}$ and $T^{\max}$ are the maximum achievable values for V_c and T_c, respectively. The Lagrangian function for this optimal control problem (59-61) is defined by

$$\begin{aligned}
L\,(E, I, V_c, T_c) = & Z_1 E(t) + Z_2 I(t) \\
& + \frac{1}{2} A_1 V_c^2(t) + \frac{1}{2} A_2 T_c^2(t).
\end{aligned} \tag{62}$$

The Hamiltonian H for the control problem is given by

$$H\,(S, E, I, R, V_c, T_c, \lambda_i, t) = L\,(E, I, V_c, T_c) + \sum_{j=1}^{4} \lambda_j g_j, \tag{63}$$

where $\lambda_j,\ j = 1, 2, 3, 4,$ are adjoint functions that must be determined appropriately. By applying Pontryagin's Maximum Principle (incorporating delays into the Hamiltonian), we derive the following theorem, which provides the necessary conditions for optimality.

Theorem 3: Given the optimal controls $V_c^*(t)$ and $T_c^*(t)$, along with the corresponding state solutions $S^*(t), E^*(t), I^*(t)$ and $R^*(t)$ of the state system (59) and (61), there exist adjoint variables $\lambda_1(t), \lambda_2(t), \lambda_3(t)$ and $\lambda_4(t)$ that satisfy the following adjoint system

$$\begin{aligned}
\dot{\lambda}_1 = & -\lambda_1 \big[-(1 - V_c)\,\sigma\beta I^* - (1 - T_c)\,(1 - \sigma)\lambda I^* \\
& -\alpha - \mu_1 \big] \\
& - \lambda_2 \big[(1 - V_c)\,\sigma\beta I^* + (1 - T_c)\,(1 - \sigma)\lambda I^* \big] - \lambda_4 \alpha, \\
\dot{\lambda}_2 = & -Z_1 - \lambda_2 \left(-\gamma - \mu - V_c^* \right) - \lambda_4 \left(\gamma + T_c^* \right) \\
& - \chi_{[0, t_f - \tau]} \left[-\lambda_2(t + \tau)\delta + \lambda_3(t + \tau)\delta \right], \\
\dot{\lambda}_3 = & -Z_2 - \lambda_1(t) \big[-(1 - V_c)\,\sigma\beta S^* \\
& - (1 - T_c)\,(1 - \sigma)\lambda S^* \big] \\
& - \lambda_2 \big[-(1 - V_c)\,\sigma\beta S^* + (1 - T_c)\,(1 - \sigma)\lambda S^* \big] \\
& - \lambda_3 \left(-\theta - \eta - \mu_3 \right) - \lambda_4(\theta) \\
& - \chi_{[0, t_- - \tau]} \left[\lambda_2(t + \tau)\delta - \lambda_3(t + \tau)\delta \right], \\
\dot{\lambda}_4 = & -\lambda_4 \left(-\mu_4 \right).
\end{aligned} \tag{64}$$

The transversality conditions are given by $\lambda_j\left(t_f\right) = 0$ for $j = 1, 2, 3, 4$. Moreover, the optimal control pair $\left(V_c^*, T_c^*\right)$ is expressed by

$$\begin{aligned}
V_c^* &= \frac{(\lambda_2 - \lambda_1)\,\sigma\beta S^* I^* + (\lambda_2 - \lambda_4)\,E^*}{A_1}, \\
T_c^* &= \frac{(\lambda_2 - \lambda_1)\,(1 - \sigma)\lambda S^* I^* + (\lambda_3 - \lambda_4)\,I^*}{A_2}.
\end{aligned} \tag{65}$$

Proof: Using Pontryagin's Maximum Principle with delay conditions, we derive the following adjoint equations and transversality conditions

$$\begin{aligned}
\dot{\lambda}_1 &= -\frac{\partial H(t)}{\partial S} - \chi_{[0, t_f - \tau]} \frac{\partial H(t + \tau)}{\partial S_\tau},\ \lambda_1\left(t_f\right) = 0, \\
\dot{\lambda}_2 &= -\frac{\partial H(t)}{\partial E} - \chi_{[0, t_f - \tau]} \frac{\partial H(t + \tau)}{\partial E_\tau},\ \lambda_2\left(t_f\right) = 0, \\
\dot{\lambda}_3 &= -\frac{\partial H(t)}{\partial I} - \chi_{[0, t_f - \tau]} \frac{\partial H(t + \tau)}{\partial I_\tau},\ \lambda_3\left(t_f\right) = 0, \\
\dot{\lambda}_4 &= -\frac{\partial H(t)}{\partial R} - \chi_{[0, t_f - \tau]} \frac{\partial H(t + \tau)}{\partial R_\tau},\ \lambda_4\left(t_f\right) = 0.
\end{aligned} \tag{66}$$

By the optimality conditions, the derivatives of the Hamiltonian with respect to the controls yield

$$\begin{aligned}
\frac{\partial H}{\partial V_c} &= A_1 V_c^* + \sigma\beta S^* I^* \lambda_1 - \lambda_2 \sigma\beta S^* I^* \\
&\quad + \lambda_4 E^* - \lambda_2 E^* = 0 \text{ at } V_c = V_c^*, \\
\frac{\partial H}{\partial T_c} &= A_2 T_c^* + \lambda_1 (1 - \sigma)\lambda S^* I^* - \lambda_2 (1 - \sigma)\lambda S^* I^* \\
&\quad - \lambda_3 I^* + \lambda_4 I^* = 0 \text{ at } T_c = T_c^*.
\end{aligned}$$

From these equations, we find that the optimal controls are expressed as

$$V_c^* = \frac{(\lambda_2 - \lambda_1)\,\sigma\beta S^* I^* + (\lambda_2 - \lambda_4)\,E^*}{A_1},$$
$$T_c^* = \frac{(\lambda_2 - \lambda_1)\,(1-\sigma)\lambda S^* I^* + (\lambda_3 - \lambda_4)\,I^*}{A_2}.$$

Using the properties of the control space, we obtain the following

$$V_c^*(t) = \begin{cases} 0, & \text{if } W(t) \le 0, \\ W(t), & \text{if } 0 < W(t) < V_c^{*\max}, \\ V_c^{*\max}, & \text{if } W(t) \ge V_c^{*\max}, \end{cases}$$

and

$$T_c^*(t) = \begin{cases} 0, & \text{if } F(t) \le 0, \\ F(t), & \text{if } 0 < F(t) < T_c^{*\max}, \\ T_c^{*\max}, & \text{if } F(t) \ge T_c^{*\max}, \end{cases}$$

where

$$F(t) = \frac{[\lambda_2(t) - \lambda_1(t)]\,(1-\sigma)\lambda S^*(t) I^*(t) + [\lambda_3(t) - \lambda_4(t)]\,I^*(t)}{A_2}$$

and

$$W(t) = \frac{[\lambda_2(t) - \lambda_1(t)]\,\sigma\beta S^*(t) I^*(t) + [\lambda_2(t) - \lambda_4(t)]\,E^*(t)}{A_1}.$$

Thus, the optimal control pair (V_c^*, T_c^*) is as described in (64). The optimal control pair and corresponding state is found by ensuring the following optimality procedures, which include state order (59), connected system (66), boundary conditions (60) and (64),

$$\begin{aligned}
\dot{S}^* &= \Pi - \left(1 - V_c^*\right)\sigma\beta S^* I^* - \left(1 - T_c^*\right)(1-\sigma)\lambda S^* I^* \\
&\quad - \alpha S^* - \mu_1 S^*, \\
\dot{E}^* &= \left(1 - V_c^*\right)\sigma\beta S^* I^* + \left(1 - T_c^*\right)(1-\sigma)\lambda S^* I^* \\
&\quad - \delta E^*(t-\tau) - \gamma E^* - \mu_2 E^* - m E^*, \\
\dot{I}^* &= \delta E^*(t-\tau) - \theta I^* - \eta I^* - \mu_3 I^* - n I^*, \\
\dot{R}^* &= \alpha S^* + \gamma E^* + \theta I^* - \mu_4 R^* + m E^* + n I^*,
\end{aligned}$$

where

$$m = \max\{M, 0\}, \quad n = \max\{N, 0\},$$

with

$$M = \min\left(\frac{(\lambda_2 - \lambda_1)\,\sigma\beta S^* I^* + (\lambda_2 - \lambda_4)\,E^*}{A_1}, V_c^{\max}\right),$$

$$N = \min\left(\frac{(\lambda_2 - \lambda_1)\,(1-\sigma)\lambda S^* I^* + (\lambda_3 - \lambda_4)\,I^*}{A_2}, T_c^{\max}\right)$$

and

$$\begin{aligned}
\dot{\lambda}_1 &= -\lambda_1\left[-\left(1 - V_c^*\right)\sigma\beta I^* - \left(1 - T_c^*\right)(1-\sigma)\lambda I^* - \alpha - \mu_1\right] \\
&\quad - \lambda_2\left[\left(1 - V_c^*\right)\sigma\beta I^* + \left(1 - T_c^*\right)(1-\sigma)\lambda I^*\right] - \lambda_4(\alpha), \\
\dot{\lambda}_2 &= -Z_1 - \lambda_2\left(-\gamma - \mu_2 - V_c^*\right) - \lambda_4\left(\gamma + V_c^*\right) \\
&\quad - \chi_{[0,t,-\tau]}\left[-\lambda_2(t+\tau)\delta + \lambda_3(t+\tau)\delta\right], \\
\dot{\lambda}_3 &= -Z_2 - \lambda_1\left[-\left(1 - V_c^*\right)\sigma\beta S^* - \left(1 - T_c^*\right)(1-\sigma)\lambda S^*\right] \\
&\quad - \lambda_2\left[\left(1 - V_c^*\right)\sigma\beta S^* + \left(1 - T_c^*\right)(1-\sigma)\lambda S^*\right] \\
&\quad - \lambda_3\left[-\theta - \eta - \mu_3 - T_c^*\right] - \lambda_4\left(\theta + T_c^*\right) \\
&\quad - \chi_{[0,t_- - \tau]}\left[\lambda_2(t+\tau)\delta - \lambda_3(t+\tau)\delta\right], \\
\dot{\lambda}_4 &= -\lambda_4(t)\,(-\mu_4),
\end{aligned}$$

with $\lambda_1(t_f) = \lambda_2(t_f) = \lambda_3(t_f) = \lambda_4(t_f) = 0$.

VI. NUMERICAL SIMULATIONS

In this section, we perform numerical simulations to validate the analytical results by carefully selecting parameter values that align with the conditions derived in earlier sections. By varying the delay values, we explore various scenarios associated with the inner equilibrium point. The parameters are chosen to satisfy the conditions established analytically in the previous sections. Specifically, we consider the system defined by

$$\begin{aligned}
\dot{S} &= 0.65 - (0.4)(0.00001)SI - (1 - 0.4)(0.0001)SI \\
&\quad - (0.0004)S - (0.00001)S, \\
\dot{E} &= (0.4)(0.00001)SI + (1 - 0.4)(0.0001)SI \\
&\quad - (0.005)E(t-\tau) - (0.004)E - (0.0001)E, \\
\dot{I} &= (0.005)E(t-\tau) - (0.006)I - (0.001)I \\
&\quad - (0.001)I.
\end{aligned} \tag{67}$$

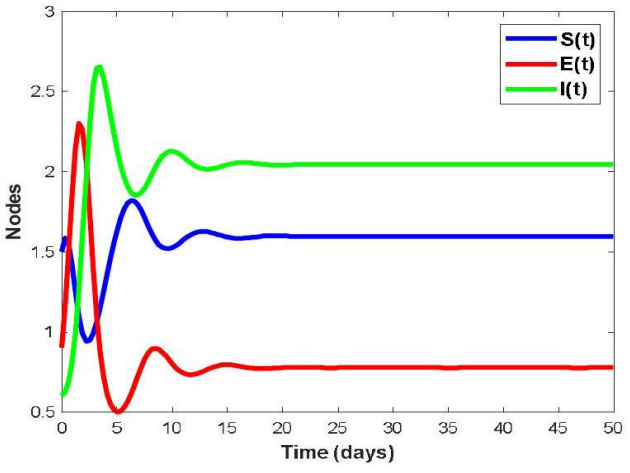

FIGURE 1. A time series plot of the node classes $S(t)$, $E(t)$ and $I(t)$, derived from system (67), with $\tau = 0$.

Figure 1 illustrates a time series analysis conducted to explore the dynamics of the system in the absence of delay.

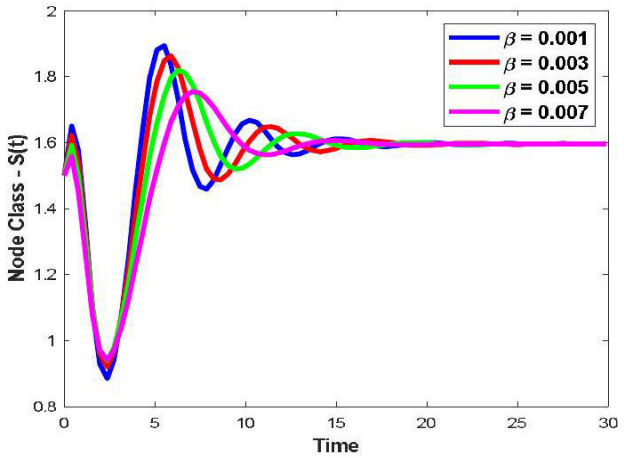

FIGURE 2. Time series projection of susceptible (S) nodes under varying worm spreading capabilities weak (β) within the IoT system modeled by system (67), with delay $\tau = 0$.

When there is no delay, the dynamics of the system remain stable for the values of the parameters chosen specified in the system (67). Meanwhile, Figure 1 displays time series plots of susceptible, exposed, and infected nodes, showing their dynamics as managed by the system (67). This forms the baseline for understanding variations in worm propagation.

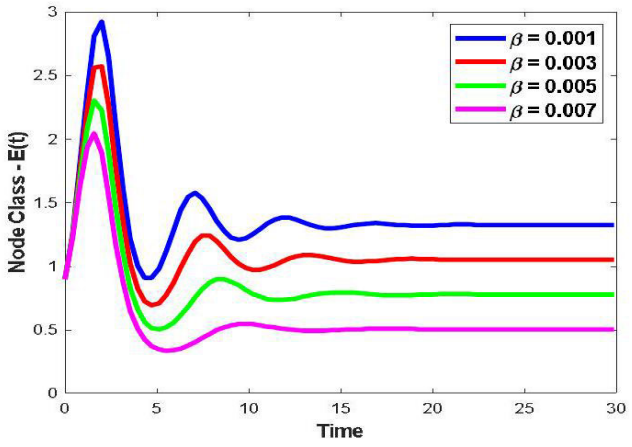

FIGURE 3. Time series projection of exposed (E) nodes under varying worm spreading capabilities weak (β), within the IoT system modeled by system (67), with delay $\tau = 0$.

Figures 2–4 depict the time series plots of susceptible, exposed, and infected nodes respectively for varying values of β, along with other parameters defined within the system (67). Figure 2 illustrates the time series variations of susceptible nodes for different values of β. As the transmission coefficient β, which represents the rate of transition from exposed to infected nodes, increases, the susceptible node population initially exhibits a slight upward trend, followed by a more noticeable increase over time. This rise is attributed to the growing number of infected nodes, which indirectly leads to an increase in the susceptible population. Figure 3

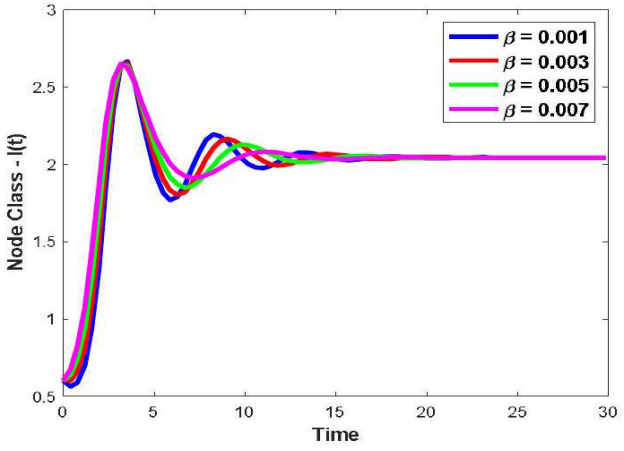

FIGURE 4. Time series projection of infected (I) nodes under varying worm spreading capabilities weak (β), within the IoT system modeled by system (67), with delay $\tau = 0$.

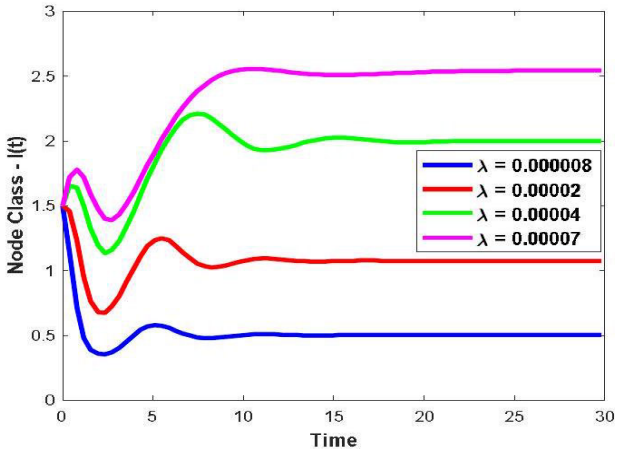

FIGURE 5. Time series projections of susceptible (S) nodes under varying worm spreading capabilities strong (λ), within the IoT system modeled by system (67), with delay $\tau = 0$.

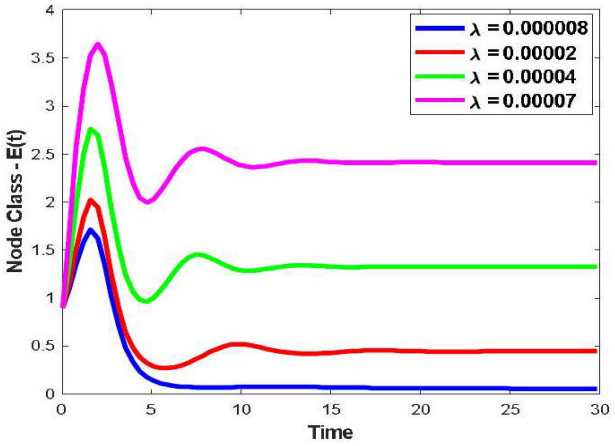

FIGURE 6. Time series projections of exposed (E) nodes under varying worm spreading capabilities strong (λ), within the IoT system modeled by system (67), with delay $\tau = 0$.

shows the time series variations of exposed nodes for different values of the transmission coefficient β, which manages the

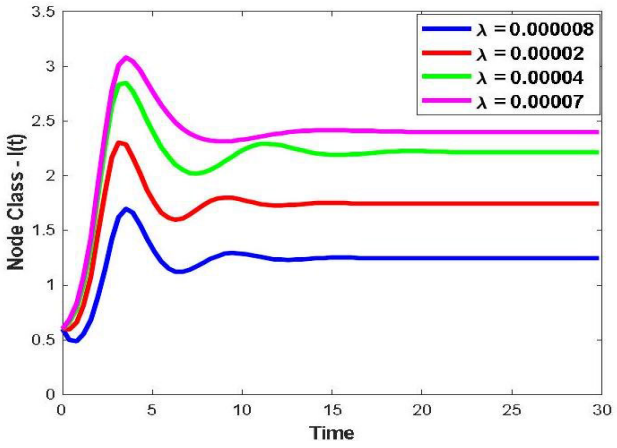

FIGURE 7. Time series projections of infected (I) nodes under varying worm spreading capabilities strong (λ), within the IoT system modeled by system (67), with delay $\tau = 0$.

transition from exposed to infected nodes. As β increases, the exposed node population demonstrates a decreasing trend. This decline occurs because a higher β accelerates the transition of exposed nodes into the infected stage, reducing the exposed node class. Figure 4 illustrates the time series variations of infected nodes for different values of β. As β increases, the population of infected nodes shows a clear upward trend, becoming increasingly prominent with higher values of β, which reflects the accelerated spread of infection within the system.

Figures 5–7 present the time series plots of susceptible, exposed, and infected nodes for various values of λ, along with the other attributes framed in the system (67). Figure 5 shows the time series variations of susceptible nodes for different values of λ. As the transmission coefficient λ, which represents the spreading capabilities of devices in the IoT system, increases, the susceptible node population exhibits a growing trend, reflecting the increasing impact of infection spread within the system (67). Figure 6 illustrates the time series variations of the exposed nodes for different values of λ. With increasing λ, the exposed node population shows a rapid upward trend, indicating that stronger spreading capabilities accelerate the transition to the exposed state within the IoT system as modeled by the system (67). Figure 7 presents the time series variations of infected nodes for various values of λ. As λ increases, the population of infected nodes shows a significant and consistent upward trend. This highlights the strong influence of high transmission coefficients in driving the growth of infection within the system (67).

These numerical studies reveal a decline in the percentage of HIoT devices infected by worms with weak spreading capabilities, while the percentage of devices infected by worms with strong spreading capabilities shows a marked increase. Furthermore, the propagation rate of malware has exceeded previous levels, significantly expanding the scope of infection, as illustrated in Figures 2–7.

The time series plots in Figures 2–4 indicate that the number of vulnerable (susceptible) nodes gradually increases, the number of exposed nodes steadily decreases, and the number of infected nodes shows a consistent upward trend within the system (67). An increase in the transmission coefficient of devices with limited spreading capacities in the IoT system drives this behavior. Furthermore, fluctuations are observed in the system's susceptible, exposed, and infected components (67) when the transmission coefficient for devices with strong spreading capabilities increases within the IoT system. These dynamics underscore the increased impact of strongly spreading worms on the system's overall stability and infection patterns.

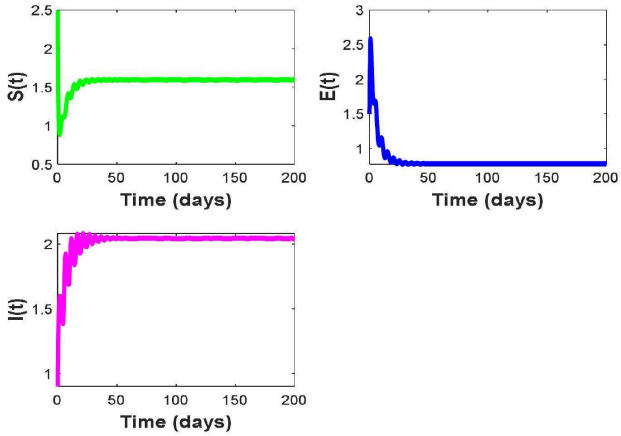

FIGURE 8. The time series plot of the node classes *S-E-I*, in an IoT system, based on the system (67), with $\tau = 4.5 < \tau_0$.

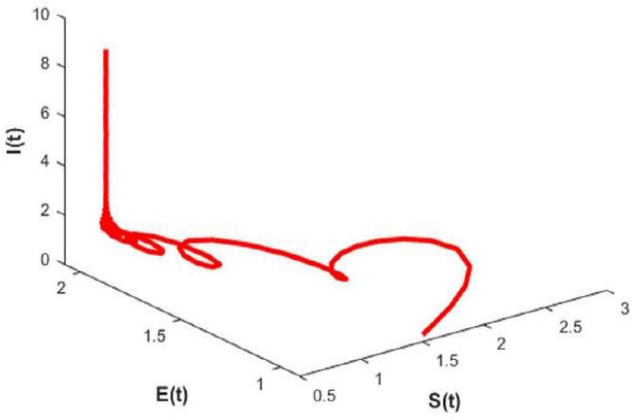

FIGURE 9. The phase portrait projections of the node classes *S-E-I*, in an IoT system, as described by the system (67), with $\tau = 4.5 < \tau_0$.

Our empirical analysis demonstrates that the spread of worms within HIoT systems can be effectively controlled, provided that latent delays remain below a critical threshold. However, when latent delays exceed this threshold, worm proliferation becomes unmanageable. Thus, maintaining control over latent delays is crucial, particularly to ensure

the direction and stability of the Hopf bifurcation when $\tau > 0$. Numerical simulations reveal the following results for $\Omega_1(0) = -0.000132 - i(0.00935)$, $\mu_2 = 23.412238 > 0$, $\beta_2 = -0.000231 < 0$, and $T_2 = -0.003736 < 0$, when $\tau = 10.5 \in [0, \tau^+]$. According to Theorem 2, we can conclude that the Hopf bifurcation is supercritical, with the resulting periodic solutions exhibiting stable behavior characterized by a decreasing period.

Given the stability of these bifurcating periodic solutions, all classes of HIoT nodes within the Internet of Things (IoT) system managed by the system (67) can coexist in an oscillatory state. However, in HIoT systems, such oscillatory behavior is undesirable. Our numerical simulations further indicate that the onset of the Hopf bifurcation and the accompanying oscillations can be delayed by appropriately adjusting the constant recruitment rate of vulnerable nodes and the recovery rate of infected nodes. Since Hopf bifurcation and oscillation tend to co-occur, we recommend that HIoT system administrators adopt effective strategies to regulate the recruitment of vulnerable nodes and ensure timely updates of antivirus software. These measures can significantly help manage the propagation of the worm within the system.

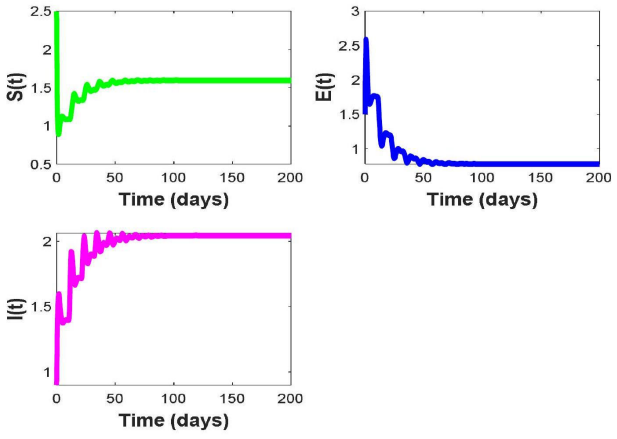

FIGURE 10. The time series plots of the node classes*S-E-I*, in an IoT system, based on system (67), with $\tau = 10.5 = \tau_0$.

Additionally, our simulations suggest that increasing certain parameter values can delay the onset of the Hopf bifurcation. Enhancing the immunity of HIoT systems connected to the IoT presents a promising approach to achieve this. Therefore, system administrators must prioritize improving the vaccination rates of HIoT systems within IoT systems. This proactive strategy is essential for accurately predicting and limiting worm propagation in HIoT systems associated with the IoT. Details are illustrated in Figures 8–13, respectively.

Figures 14–17 show the time series plots of susceptible, exposed infected, and recovered nodes under optimal control values $V_c = 0$, $T_c = 0$ and $V_c = 0.003$, $T_c = 0.005$, along with the other attributes defined in the system (67).

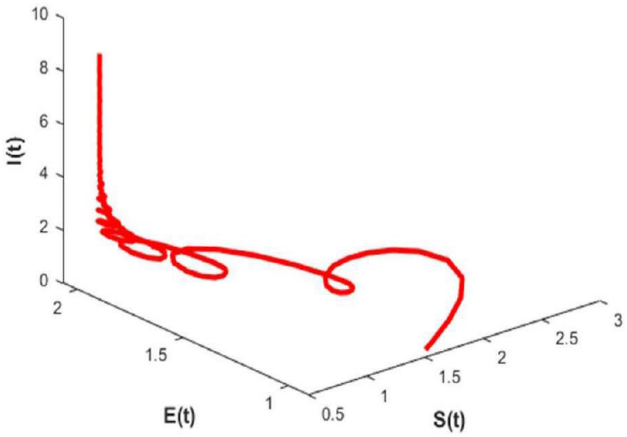

FIGURE 11. The phase portrait projections of the node classes *S-E-I*, in an IoT system, as modeled by the system (67), with $\tau = 10.5 = \tau_0$.

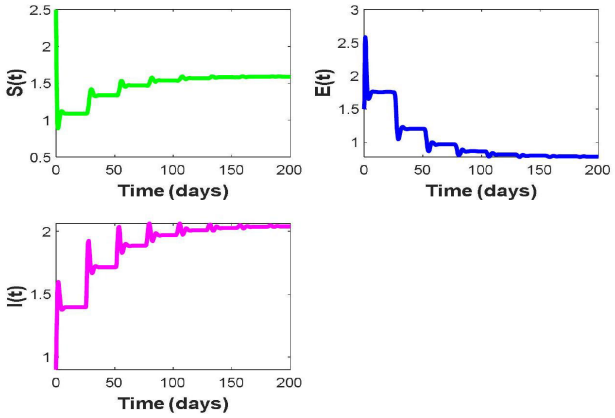

FIGURE 12. The time series plots of the node classes *S-E-I*, in an IoT system, as modeled by the system (67), with $\tau = 25.5 > \tau_0$.

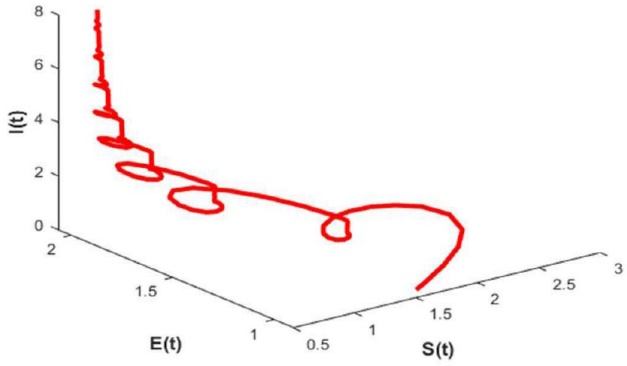

FIGURE 13. The phase portrait projections of the node classes *S-E-I*, in an IoT system, as described by the system (67), with $\tau = 25.5 > \tau_0$.

Figure 14 illustrates that the susceptible node class S increases in the absence of control parameters (i.e. $V_c = 0$ and $T_c = 0$), but decreases when control measures (i.e. $V_c = 0.003$ and $T_c = 0.005$) are implemented.

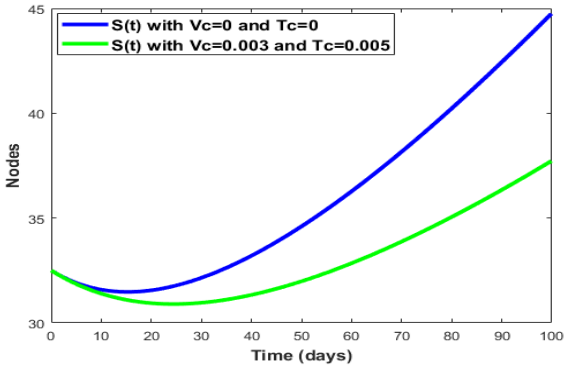

FIGURE 14. The time series plots of the node class S in an IoT system, as described by the system (67), with $V_c = 0$, $T_c = 0$ and $V_c = 0.003$, $T_c = 0.005$.

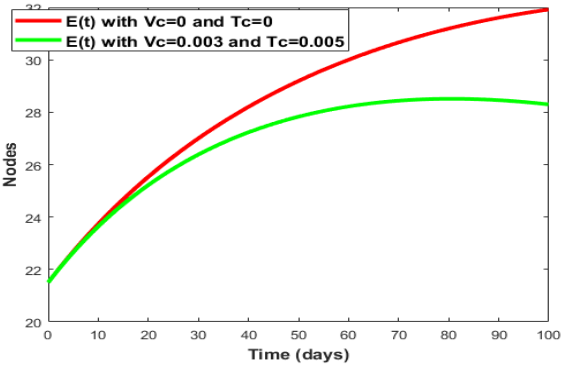

FIGURE 15. The time series plots of the node class E in an IoT system, as described by the system (67), with $V_c = 0$, $T_c = 0$ and $V_c = 0.003$, $T_c = 0.005$.

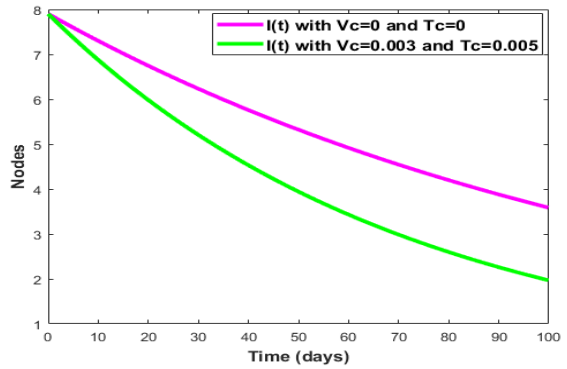

FIGURE 16. The time series plots of the node class I in an IoT system, as described by the system (67), with $V_c = 0$, $T_c = 0$ and $V_c = 0.003$, $T_c = 0.005$.

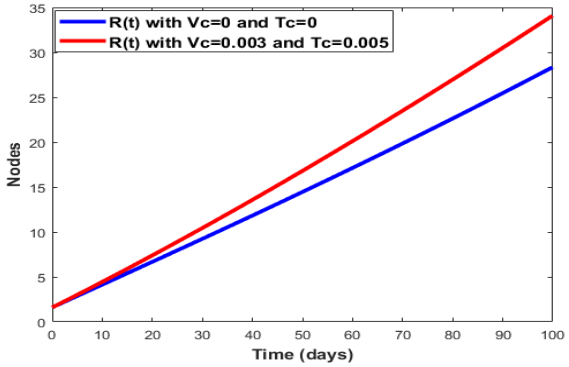

FIGURE 17. The time series plots of the node class R in an IoT system, as described by the system (67), with $V_c = 0$, $T_c = 0$ and $V_c = 0.003$, $T_c = 0.005$.

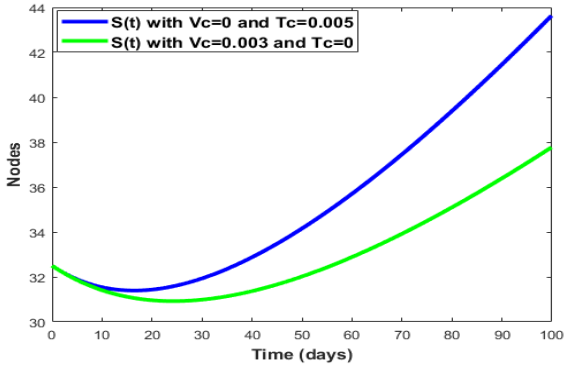

FIGURE 18. The time series plots of the node class S in an IoT system, as described by the system (67), with $V_c = 0$, $T_c = 0.005$ and $V_c = 0.003$, $T_c = 0$.

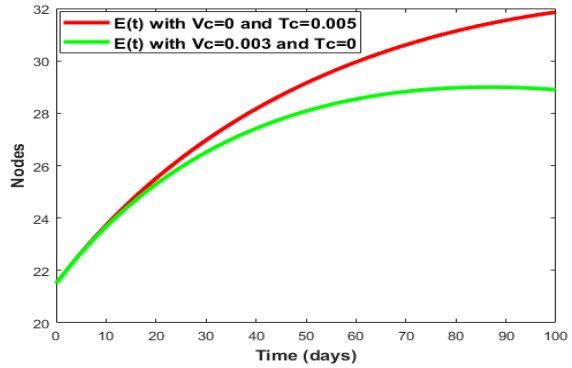

FIGURE 19. The time series plots of the node class E in an IoT system, as described by the system (67), with $V_c = 0$, $T_c = 0.005$ and $V_c = 0.003$, $T_c = 0$.

This demonstrates the effectiveness of control parameters in mitigating infections.

Figures 14 and 16 show that the exposed E and infected I node classes increase in the absence of control parameters (i.e. $V_c = 0$ and $T_c = 0$), but decrease in the presence of control parameters (i.e. $V_c = 0.003$ and $T_c = 0.005$). The control parameters effectively regulate the spread and infectious potential, highlighting the significant impact of the optimal control strategy on the proposed model.

Figure 17 illustrates that recovered node class R exhibits an increasing trend in the presence of control parameters (i.e. $V_c = 0.003$ and $T_c = 0.005$), and a decreasing trend in the absence of control parameters (i.e. $V_c = 0$ and $T_c = 0$). The

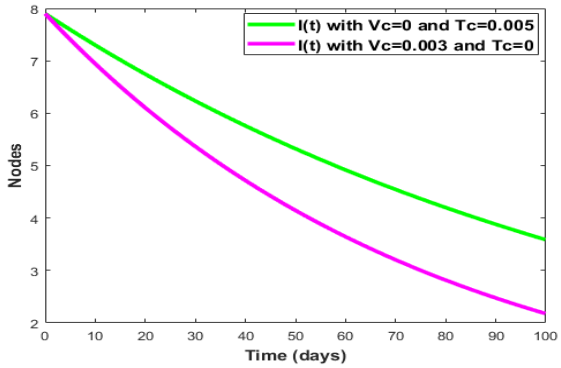

FIGURE 20. The time series plots of the node class I in an IoT system, as described by the system (67), with $V_c = 0$, $T_c = 0.005$ and $V_c = 0.003$, $T_c = 0$.

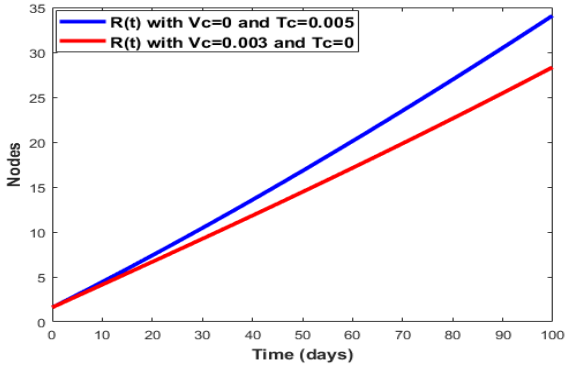

FIGURE 21. The time series plots of the node class R in an IoT system, as described by the system (67), with $V_c = 0$, $T_c = 0.005$ and $V_c = 0.003$, $T_c = 0$.

control parameters can work effectively in the recovery stage and are also one of the notable effects of the proposed model.

Figures 18–21 present the time series plots of susceptible, exposed, infected, and recovered nodes under different control parameter combinations ($V_c = 0$, $T_c = 0.005$ and $V_c = 0.003$, $T_c = 0$), along with the other attributes framed in the system (67). The results indicate that the susceptible and exposed node classes increase in the absence of vaccination control $V_c = 0$, even when treatment measures $T_c = 0.005$ are in place. This suggests that treatment alone is insufficient to control infection spread without preventive measures such as firewalls, antivirus software, or security filters. Vaccination control strategies play a crucial role in minimizing the destructive effects of malware. Implementing preventive security measures alongside treatment strategies is essential to effectively control worm propagation in HIoT systems

VII. COMPARATIVE STUDY

In this section, we compare the numerical results of the Caputo-Fabrizio fractional-order derivatives with those of the integer-order derivative by the motivation of [41], [42], [43], [44], [45], [46], [47], [48], *and*[49]. The proposed model with Caputo-Fabrizio fractional order derivatives as follows:

$$^{CF}D_t^{\xi} S = \Pi^{\xi} - \sigma^{\xi}\beta^{\xi} SI - (1-\sigma^{\xi})\lambda^{\xi} SI - \alpha^{\xi} S - \mu_1^{\xi} S. \tag{68}$$

$$^{CF}D_t^{\xi} E = \sigma^{\xi}\beta^{\xi} SI + (1-\sigma^{\xi})\lambda^{\xi} SI - \delta^{\xi} E(t-\tau) - \gamma^{\xi} E - \mu_2^{\xi} E. \tag{69}$$

$$^{CF}D_t^{\xi} I = \delta^{\xi} E(t-\tau) - \theta^{\xi} I - \eta^{\xi} I - \mu_3^{\xi} I. \tag{70}$$

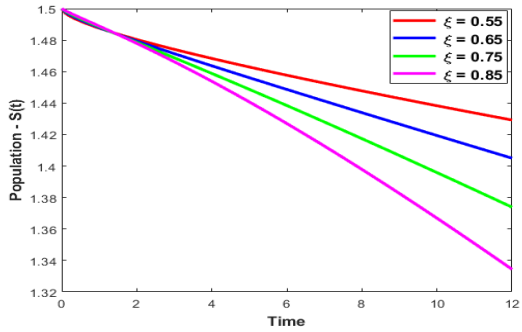

FIGURE 22. The time series plots of the node class S framed in the system (68)-(70), with the variation of ξ as 0.55,0.65,0.75,0.85.

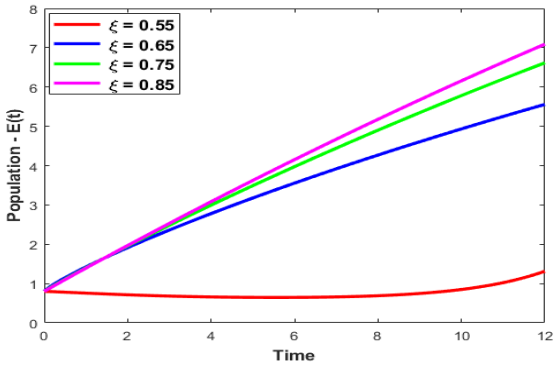

FIGURE 23. The time series plots of the node class E framed in the system (68)-(70), with the variation of ξ as 0.55,0.65,0.75,0.85.

As the approximate solutions tend to the classic integer solution with $\xi = 1$, Figures 22–24 demonstrate that the dynamics of the system (68)-(70) are significantly impacted by different fractional orders and indicate that as fractional order tends to one. Additionally, Figures 22–24 demonstrate that while each function behaves the same for a range of values, the results obtained for these values vary. Tables 1–3 also provide a comparison between the integer order and the non-integer-order model. The results of the integer and fractional order for the three state nodes S, E, and I functions in Tables 1–3 show that they behave similarly in Caputo-Fabrizio derivatives, but their values differ, and this difference is not consistent. At certain points, the fractional-order Caputo derivative's value is closer to the integer order result, and at other points, the fractional-order

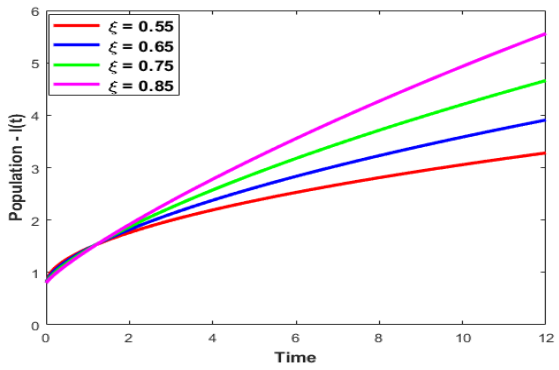

FIGURE 24. The time series plots of the node class *I* framed in the system (68)-(70), with the variation of ξ as 0.55,0.65,0.75,0.85.

Caputo-Fabrizio derivative's result is closer to the integer order result.

TABLE 1. Comparison between ordinary derivative and Caputo-Fabrizio fractional derivative for susceptible node.

Time (t)	0	1	2	3	4
D^{ξ}	1.5	1.50018	1.52846	1.53895	1.54001
${}^{CF}D^{\xi}$	1.50011	1.50093	1.52879	1.53991	1.54621

TABLE 2. Comparison between ordinary derivative and Caputo-Fabrizio fractional derivative for exposed node.

Time (t)	0	1	2	3	4
D^{ξ}	1	1.13854	1.19587	1.28491	1.30057
${}^{CF}D^{\xi}$	1.0017	1.15467	1.21482	1.29447	1.34548

TABLE 3. Comparison between ordinary derivative and Caputo-Fabrizio fractional derivative for infected node.

Time (t)	0	1	2	3	4
D^{ξ}	1	1.10074	1.15648	1.21861	1.26843
${}^{CF}D^{\xi}$	1.0004	1.00954	1.11681	1.19586	1.22418

Figures show the asymptotic behavior of the worm propagation in heterogeneous IoT network system without treatment, for different values of in the Caputo-Fabrizio operator. In addition, the responses within the Caputo-Fabrizio fractional model tend to the integer response as goes to 1. However, as is known, fractional differentiation introduces additional complexity in the modeling of real-world dynamics. In contrast, the main advantage of this approach is to describe the complex behavior of such systems more accurately than the pre-existing classical models with integer-order derivatives.

Figures 22–24 show that time series plots for various fractional order values which are quite interesting and inspiring lead to future studies on fractional order modeled systems. Particularly, the simulation results favor towards the accurate model and optimal control strategies. The current proposed model (3) is designed to study the delay dynamics and optimal control strategies for an IoT system. The next study will be on Caputo-Frabrizio fractional order modeling with optimal control strategies. As the simulation results, Figures 22–24 achieved the aim of the fractional model with optimal control. Figure 22 says for a lower fractional order value $S(t)$ is more. Figure 24 says that the lower fractional order value $I(t)$ is less and follows the decreasing trend. So at lower values of fractional order, we can achieve the aim to minimize the infection and provide better solutions to control the malware spread. The literatures [41], [42], [43], [44], [45], [46], [47], [48], [49], and [50] motivates and guides us to study the Caputo-Fabrizio model dynamics with different mathematical tools and techniques. The effective workflow and simulation in [50] inspire us for this comparative study to make this analysis more informative.

VIII. CONCLUDING REMARKS

This study investigated the propagation of worms in HIoT systems across various threshold values to determine the optimal parameter for managing the delay duration required for system stabilization. The study aimed to identify latency-infected parameters that efficiently control delay time, ensure system stabilization, and mitigate the negative consequences of worm outbreaks by systematically assessing these thresholds. The findings underscore the importance of regulating oscillatory behavior in the propagation of worms and highlight the need for targeted interventions to prevent long-term instability in HIoT contexts. In particular, this paper presents an optimal policy implementation to effectively reduce the propagation of worms and minimize the number of devices exposed and infected. Optimal vaccination and treatment strategies were analyzed using Pontryagin's maximum principle for both weak and strong spreading outbreaks, applying time-limited treatment within a delayed HSEIR model. Building on these findings, further investigation into worm propagation in large-scale networks with various system configurations should broaden the scope of the study. A more comprehensive understanding of worm infestations in complex real-world IoT environments can be achieved by incorporating additional factors such as computational power and device mobility. Including these parameters would enhance the applicability of the model and provide more reliable mitigation techniques to protect next-generation IoT infrastructures. Future work should extend the findings to various systems, considering additional parameters like computing capacity and mobility in large-scale networks. Furthermore, secure environments, such as blockchain-enabled networks, should be incorporated into future studies. Future research by the author collective will focus on developing a suitable architecture for studying complex phenomena. Two particularly promising areas of research, fractional-order modeling, and comparative analysis, are expected to play a pivotal role in advancing Industry 4.0 and 5.0.

REFERENCES

[1] Abu, Brown, Eric. (2016). *Who Needs the Internet of Things*. [Online]. Available: https://www.linux.com/news/who-needs-internetthings

[2] S. Kumar, P. Tiwari, and M. Zymbler, "Internet of Things is a revolutionary approach for future technology enhancement: A review," *J. Big Data*, vol. 6, no. 1, pp. 1–21, Dec. 2019.

[3] L. Li, J. Cui, R. Zhang, H. Xia, and X. Cheng, "Dynamics of complex networks: Malware propagation modeling and analysis in industrial Internet of Things," *IEEE Access*, vol. 8, pp. 64184–64192, 2020.

[4] D. Acarali, M. Rajarajan, N. Komninos, and B. B. Zarpelão, "Modelling the spread of botnet malware in IoT-based wireless sensor networks," *Secur. Commun. Netw.*, vol. 2019, pp. 1–13, Feb. 2019.

[5] J. N. C. Gonçalves, H. S. Rodrigues, and M. T. T. Monteiro, "Optimal control measures for a susceptible-carrier-infectious-recovered-susceptible malware propagation model," *Optim. Control Appl. Methods*, vol. 40, no. 4, pp. 691–702, Jul. 2019.

[6] R. Dhineshbabu, J. Alzabut, A. G. M. Selvam, S. Etemad, and S. Rezapour, "Modeling and qualitative dynamics of the effects of internal and external storage device in a discrete fractional computer virus," *Qualitative Theory Dyn. Syst.*, vol. 23, no. 4, Sep. 2024, Art. no. 182.

[7] T. Jabeen, I. Jabeen, H. Ashraf, N. Z. Jhanjhi, A. Yassine, and M. S. Hossain, "An intelligent healthcare system using IoT in wireless sensor network," *Sensors*, vol. 23, no. 11, 2023, Art. no. 5055.

[8] I. F. Akyildiz, W. Su, Y. S. Subramaniam, and E. Cayirci, "Wireless sensor networks: A survey," *Comput. Netw.*, vol. 38, pp. 393–422, Mar. 2022.

[9] S. Shen, H. Zhou, S. Feng, J. Liu, H. Zhang, and Q. Cao, "An epidemiology-based model for disclosing dynamics of malware propagation in heterogeneous and mobile WSNs," *IEEE Access*, vol. 8, pp. 43876–43887, 2020.

[10] Z. Huanan, X. Suping, and W. Jiannan, "Security and application of wireless sensor network," *Proc. Comput. Sci.*, vol. 183, pp. 486–492, Jan. 2021.

[11] A. Seyfollahi, M. Moodi, and A. Ghaffari, "MFO-RPL: A secure RPL-based routing protocol utilizing moth-flame optimizer for the IoT applications," *Comput. Standards Interface*, vol. 82, Aug. 2022, Art. no. 103622.

[12] Q. Gao and J. Zhuang, "Stability analysis and control strategies for worm attack in mobile networks via a VEIQS propagation model," *Appl. Math. Comput.*, vol. 368, Mar. 2020, Art. no. 124584.

[13] A. Ullah, M. Azeem, H. Ashraf, A. A. Alaboudi, M. Humayun, and N. Jhanjhi, "Secure healthcare data aggregation and transmission in IoT—A survey," *IEEE Access*, vol. 9, pp. 16849–16865, 2021.

[14] J. Wu, W. Jiang, Y. Mei, Y. Zhou, and T. Wang, "A survey on the progress of testing techniques and methods for wireless sensor networks," *IEEE Access*, vol. 7, pp. 4302–4316, 2019.

[15] M. J. Farooq and Q. Zhu, "Modeling, analysis, and mitigation of dynamic botnet formation in wireless IoT networks," *IEEE Trans. Inf. Forensics Security*, vol. 14, no. 9, pp. 2412–2426, Sep. 2019.

[16] H. ElSawy, M. A. Kishk, and M.-S. Alouini, "Spatial firewalls: Quarantining malware epidemics in large-scale massive wireless networks," *IEEE Commun. Mag.*, vol. 58, no. 9, pp. 32–38, Sep. 2020.

[17] Y. Li, G. Xu, H. Xian, L. Rao, and J. Shi, "Novel Android malware detection method based on multi-dimensional hybrid features extraction and analysis," *Intell. Autom. Soft Comput.*, vol. 25, no. 3, pp. 637–647, 2019.

[18] C. Du, S. Liu, L. Si, Y. Guo, and T. Jin, "Using object detection network for malware detection and identification in network traffic packets," *Comput., Mater. Continua*, vol. 64, no. 3, pp. 1785–1796, 2020.

[19] N. Keshri and B. K. Mishra, "Two time-delay dynamic model on the transmission of malicious signals in wireless sensor network," *Chaos, Solitons Fractals*, vol. 68, pp. 151–158, Nov. 2014.

[20] Z. Zhang, S. Kumari, and R. K. Upadhyay, "A delayed e-epidemic SLBS model for computer virus," *Adv. Difference Equ.*, vol. 2019, no. 1, Dec. 2019, Art. no. 414.

[21] T. Zhao, Z. Zhang, and R. K. Upadhyay, "Delay-induced Hopf bifurcation of an SVEIR computer virus model with nonlinear incidence rate," *Adv. Difference Equ.*, vol. 2018, no. 1, Dec. 2018, Art. no. 256.

[22] C. Wang and S. Chai, "Hopf bifurcation of an SEIRS epidemic model with delays and vertical transmission in the network," *Adv. Difference Equ.*, vol. 2016, no. 1, Dec. 2016, Art. no. 100.

[23] K. A. Khan, B. S. N. Murthy, V. Madhusudanan, M. N. Srinivas, and A. Zeb, "Hopf-bifurcation of a two delayed social networking game addiction model with graded infection rate," *Chaos, Solitons Fractals*, vol. 182, May 2024, Art. no. 114798.

[24] Q. Yan, L. Song, C. Zhang, J. Li, and S. Feng, "Modeling and control of malware propagation in wireless IoT networks," *Secur. Commun. Netw.*, vol. 2021, pp. 1–13, Jun. 2021.

[25] Z. Zhang, V. Madhusudanan, and B. S. N. Murthy, "Effect of delay in SMS worm propagation in mobile network with saturated incidence rate," *Wireless Pers. Commun.*, vol. 131, no. 1, pp. 659–678, Jul. 2023.

[26] V. Madhusudanan, M. N. Srinivas, C. H. Nwokoye, B. S. N. Murthy, and S. Sridhar, "HOPF- bifurcation analysis of delayed computer virus model with Holling type iii incidence function and treatment," *Sci. Afr.*, vol. 15, Mar. 2022, Art. no. e01125.

[27] V. Madhusudanan, M. N. Srinivas, B. S. N. Murthy, K. J. Ansari, A. Zeb, A. Althobaiti, and Y. Sabbar, "The influence of time delay and Gaussian white noise on the dynamics of tobacco smoking model," *Chaos, Solitons Fractals*, vol. 173, Aug. 2023, Art. no. 113616.

[28] V. Madhusudanan, R. Geetha, B. S. N. Murthy, N.-N. Dao, and S. Cho, "Analysis of delay-aware worm propagation model in wireless IoT systems with ratio-dependent functional response," *IEEE Access*, vol. 11, pp. 34968–34976, 2023.

[29] T. Zhao, S. Wei, and D. Bi, "Hopf bifurcation of a computer virus propagation model with two delays and infectivity in latent period," *Syst. Sci. Control Eng.*, vol. 6, no. 1, pp. 90–101, Jan. 2018.

[30] B. D. Hassard, N. D. Kzarinoff, and Y. H. Wan, *Theory and Applications of Hopf Bifurcation*. Cambridge, U.K.: Cambridge Univ. Press, 1981.

[31] C. Bianca and L. Guerrini, "Existence of limit cycles in the solow model with delayed-logistic population growth," *Sci. World J.*, vol. 2014, no. 1, pp. 1–8, 2014.

[32] M. Ferrara, L. Guerrini, and G. M. Bisci, "Center manifold reduction and perturbation method in a delayed model with a mound-shaped cobb-douglas production function," *Abstract Appl. Anal.*, vol. 2013, no. 1, pp. 1–6, 2013.

[33] S. Rezapour, V. Madhusudanan, L. Guerrini, B. S. N. Murthy, M. N. Srinivas, and S. Etemad, "A study on the qualitative properties for effects of two delays on dynamical behaviors of HIV-AIDS-TB model," *J. Appl. Math. Comput.*, Nov. 2024. [Online]. Available: https://doi.org/10.1007/s12190-024-02282-2

[34] W. Ou, C. Xu, Q. Cui, Y. Pang, Z. Liu, J. Shen, M. Z. Baber, M. Farman, and S. Ahmad, "Hopf bifurcation exploration and control technique in a predator-prey system incorporating delay," *AIMS Math.*, vol. 9, no. 1, pp. 1622–1651, 2023.

[35] H. Freedman and V. RAO, "The trade-off between mutual interference and time lags in predator-prey systems," *Bull. Math. Biol.*, vol. 45, no. 6, pp. 991–1004, 1983.

[36] H. Nyquist, "Regeneration theory," *Bell Syst. Tech. J.*, vol. 11, no. 1, pp. 126–147, Jan. 1932.

[37] M. T. Jafar, L.-X. Yang, G. Li, and X. Yang, "Optimal control of malware propagation in IoT networks," 2024, *arXiv:2401.11076*.

[38] J. Bi, S. He, F. Luo, W. Meng, L. Ji, and D.-W. Huang, "Defense of advanced persistent threat on industrial Internet of Things with lateral movement modeling," *IEEE Trans. Ind. Informat.*, vol. 19, no. 9, pp. 9619–9630, Sep. 2023.

[39] A. M. S. Mahdy and D. S. Mohamed, "Numerical simulation and dynamical system for solving biomathematical model with optimal control," *Franklin Open*, vol. 10, Mar. 2025, Art. no. 100218.

[40] A. M. S. Mahdy, "Numerical solution and optimal control for fractional tumor immune model," *J. Appl. Anal. Comput.*, vol. 14, no. 5, pp. 3033–3045, 2024.

[41] D. Baleanu, S. Etemad, H. Mohammadi, and S. Rezapour, "A novel modeling of boundary value problems on the glucose graph," *Commun. Nonlinear Sci. Numer. Simul.*, vol. 100, Sep. 2021, Art. no. 105844.

[42] D. Baleanu, A. Jajarmi, H. Mohammadi, and S. Rezapour, "A new study on the mathematical modelling of human liver with Caputo–Fabrizio fractional derivative," *Chaos, Solitons Fractals*, vol. 134, May 2020, Art. no. 109705.

[43] N. H. Tuan, H. Mohammadi, and S. Rezapour, "A mathematical model for COVID-19 transmission by using the caputo fractional derivative," *Chaos, Solitons Fractals*, vol. 140, Nov. 2020, Art. no. 110107.

[44] M. Ahmad, A. Zada, M. Ghaderi, R. George, and S. Rezapour, "On the existence and stability of a neutral stochastic fractional differential system," *Fractal Fractional*, vol. 6, no. 4, p. 203, Apr. 2022.

[45] A. M. S. Mahdy, N. H. Sweilam, and M. Higazy, "Approximate solution for solving nonlinear fractional order smoking model," *Alexandria Eng. J.*, vol. 59, no. 2, pp. 739–752, Apr. 2020.

[46] A. M. S. Mahdy, "Stability, existence, and uniqueness for solving fractional glioblastoma multiforme using a Caputo–Fabrizio derivative," *Math. Methods Appl. Sci.*, vol. 48, no. 7, pp. 7360–7377, May 2025.
[47] A. El-Mesady, A. A. Elsadany, A. M. S. Mahdy, and A. Elsonbaty, "Nonlinear dynamics and optimal control strategies of a novel fractional-order lumpy skin disease model," *J. Comput. Sci.*, vol. 79, Jul. 2024, Art. no. 102286.
[48] S. A. M. Abdelmohsen, D. S. Mohamed, H. A. Alyousef, M. R. Gorji, and A. M. S. Mahdy, "Mathematical modeling for solving fractional model cancer bosom malignant growth," *AIMS Biophys.*, vol. 10, no. 3, pp. 263–280, 2023.
[49] S. M. Aydogan, D. Baleanu, H. Mohammadi, and S. Rezapour, "On the mathematical model of rabies by using the fractional Caputo–Fabrizio derivative," *Adv. Difference Equ.*, vol. 2020, no. 1, Dec. 2020, Art. no. 382.

B. S. N. MURTHY received the Ph.D. degree in mathematics from JNTUK, Kakinada, in 2018. Since then, he has been on mathematical modeling and published various research articles in many international journals. He is currently an Associate Professor with Aditya University, Surampalem. His research interests include differential equations, computational dynamics, and wireless sensor networks.

V. MADHUSUDANAN received the Ph.D. degree from Annamalai University, Chidambaram, in 2017. He is currently an Associate Professor with the Department of Mathematics, S. A. Engineering College. He has a vast teaching and research experience in the field of mathematics and computer science. He has published many articles in various reputed national and international journals. His research interests include mathematical modeling, computational intelligence, and control systems.

M. N. SRINIVAS is currently an Associate Professor of mathematics with Vellore Institute of Technology, Vellore, India. He has about 22 years of experience in academics and has published 101 research articles in various national and international journals. He also produced one Ph.D. and guiding one scholar. His major research interests include mathematical biology and ecology modeling, stability analysis, disease models, modeling of computer virus related, graph theory, and applications of lattice theory.

L. GUERRINI received the M.A. and Ph.D. degrees in mathematics from the University of California, Los Angeles, USA. He is currently a Full Professor of mathematical economics with the Polytechnic University of Marche, Italy. He has published extensively in internationally refereed journals. His research interests include pure and applied mathematics and mathematical economics.

ANWAR ZEB received the Ph.D. degree from the University of Malakand, where he delved deep into the intersection of mathematics and biology. Subsequently, he completed a Postdoctoral Fellowship from Universidad a Distancia de Madrid (UDIMA), Spain, further honing his expertise. He is a Distinguished Scholar in the field of mathematical biology, renowned for his groundbreaking research and extensive publication record. Throughout his illustrious career, he has authored more than 150 scholarly articles in reputable journals, contributing significantly to the advancement of knowledge in his field.

NHU-NGOC DAO (Senior Member, IEEE) received the B.S. degree in electronics and telecommunications from the Posts and Telecommunications Institute of Technology, Hanoi, Vietnam, in 2009, and the M.S. and Ph.D. degrees in computer science from the School of Computer Science and Engineering, Chung-Ang University, Seoul, South Korea, in 2016 and 2019, respectively. He is currently an Assistant Professor with the Department of Computer Science and Engineering, Sejong University, Seoul. Prior to joining Sejong University, he was a Visiting Researcher with the University of Newcastle, Callaghan, NSW, Australia, in 2019, and a Postdoctoral Researcher with the Institute of Computer Science, University of Bern, Switzerland, from 2019 to 2020. He was a Visiting Professor with Chung-Ang University, from 2023 to 2024. His research interests include system softwarization, mobile cloudization, intelligent systems, and the Intelligence of Things. He is a member of ACM. He is an Editor of *ICT Express*, *Scientific Reports*, and *PLOS One* journals.

SUNGRAE CHO received the B.S. and M.S. degrees in electronics engineering from Korea University, Seoul, South Korea, in 1992 and 1994, respectively, and the Ph.D. degree in electrical and computer engineering from Georgia Institute of Technology, Atlanta, GA, USA, in 2002. He is currently a Professor with the School of computer sciences and Engineering, Chung-Ang University (CAU), Seoul. Before joining CAU, he was an Assistant Professor with the Department of Computer Sciences, Georgia Southern University, Statesboro, GA, from 2003 to 2006, and a Senior Member of Technical Staff with Samsung Advanced Institute of Technology (SAIT), Kiheung, South Korea, in 2003. From 1994 to 1996, he was a Research Staff Member with the Electronics and Telecommunications Research Institute (ETRI), Daejeon, South Korea. From 2012 to 2013, he held a Visiting Professorship with the National Institute of Standards and Technology (NIST), Gaithersburg, MD, USA. His current research interests include HIoT systeming, ubiquitous computing, and ICT convergence. He has served numerous international conferences as an organizing committee chair, such as IEEE SECON, ICOIN, ICTC, ICUFN, TridentCom, and IEEE MASS, and as a Program Committee Member, such as IEEE ICC, GLOBECOM, VTC, MobiApps, HIoTNETS, and WINSYS. He has been a Subject Editor of *IET Electronics Letter*, since 2018. He was an Area Editor of *Ad Hoc Networks* Journal (Elsevier), from 2012 to 2017.